



HAL
open science

Fluid Pulses During Stepwise Brecciation at Intermediate Subduction Depths (Monviso Eclogites, W. Alps): First Internally Then Externally Sourced

Michele Locatelli, Anne Verlaguet, Philippe Agard, T. Pettke, L. Federico

► **To cite this version:**

Michele Locatelli, Anne Verlaguet, Philippe Agard, T. Pettke, L. Federico. Fluid Pulses During Stepwise Brecciation at Intermediate Subduction Depths (Monviso Eclogites, W. Alps): First Internally Then Externally Sourced. *Geochemistry, Geophysics, Geosystems*, 2019, 20, pp.5285-5318. 10.1029/2019GC008549 . insu-03642006

HAL Id: insu-03642006

<https://insu.hal.science/insu-03642006>

Submitted on 14 Apr 2022

HAL is a multi-disciplinary open access archive for the deposit and dissemination of scientific research documents, whether they are published or not. The documents may come from teaching and research institutions in France or abroad, or from public or private research centers.

L'archive ouverte pluridisciplinaire **HAL**, est destinée au dépôt et à la diffusion de documents scientifiques de niveau recherche, publiés ou non, émanant des établissements d'enseignement et de recherche français ou étrangers, des laboratoires publics ou privés.

Copyright

Geochemistry, Geophysics, Geosystems

RESEARCH ARTICLE

10.1029/2019GC008549

Key Points:

- Mylonitic metagabbros cemented by unfoliated Omp + Grt ± Lws matrices show that pristine brecciation may occur at eclogitic conditions
- Geochemical variations and sharp increase in fluid content of matrices points to local embrittlement prior to external fluids ingression
- Structural and geochemical evidence suggest that eclogite-facies brecciation can control initial strain localization within HP shear zones

Supporting Information:

- Supporting Information S1

Correspondence to:

M. Locatelli,
locatellimichel@me.com

Citation:

Locatelli, M., Verlaquet, A., Agard, P., Pettke, T., & Federico, L. (2019). Fluid pulses during stepwise brecciation at intermediate subduction depths (Monviso eclogites, W. Alps): first internally then externally sourced. *Geochemistry, Geophysics, Geosystems*, 20, 5285–5318. <https://doi.org/10.1029/2019GC008549>

Received 10 JUL 2019

Accepted 26 OCT 2019

Accepted article online 6 NOV 2019

Published online 25 NOV 2019

©2019. American Geophysical Union.
All Rights Reserved.

Fluid Pulses During Stepwise Brecciation at Intermediate Subduction Depths (Monviso Eclogites, W. Alps): First Internally Then Externally Sourced

Michele Locatelli¹ , A. Verlaquet¹, P. Agard¹, T. Pettke², and L. Federico³

¹Istep, Sorbonne Université, Paris, France, ²Institute of Geological Sciences, University of Bern, Bern, Switzerland,

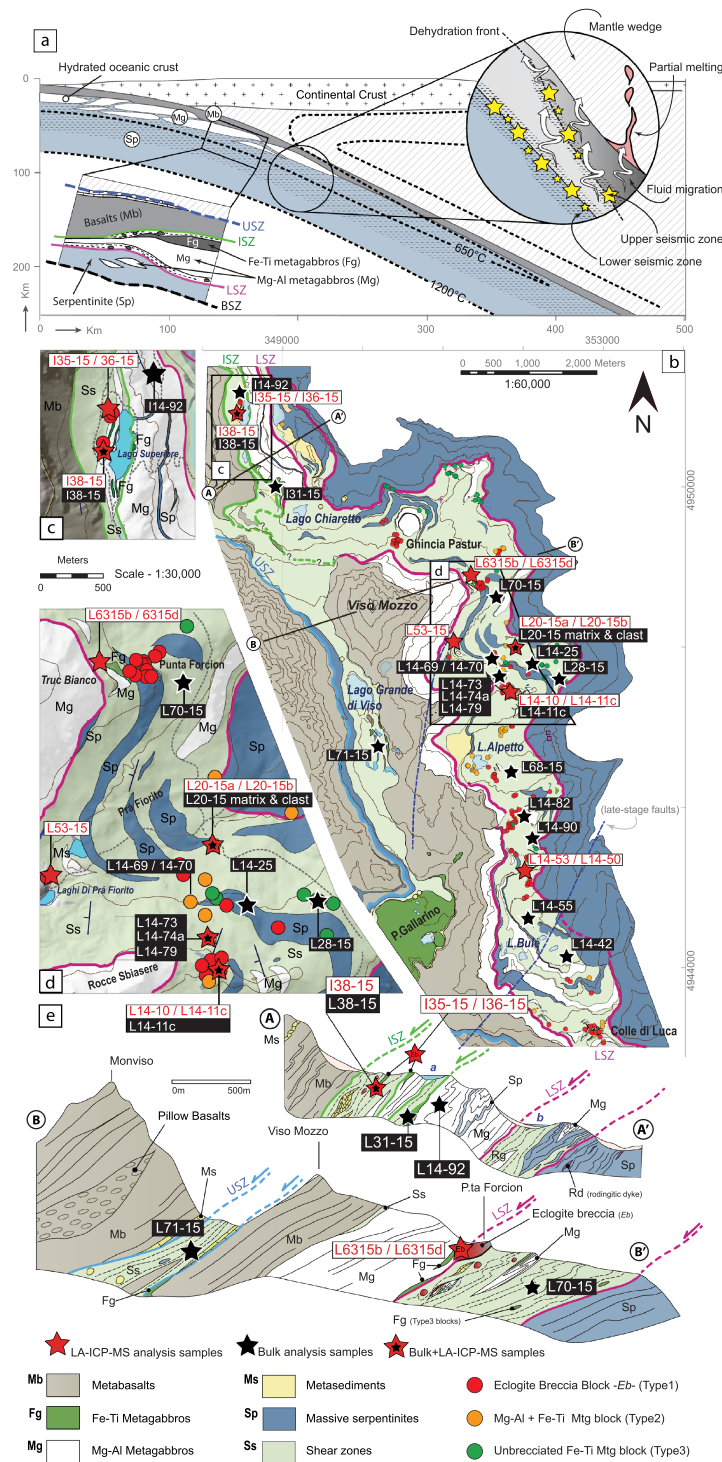
³DISTAV, Università di Genova, Genoa, Italy

Abstract Eclogite-facies breccias from the Monviso metaophiolite complex (N-Italy and W-Alps) represent a unique opportunity to study the triggering mechanisms for transient brittle deformation at eclogite-facies conditions in ductilely deforming subducted oceanic lithosphere. Here the intact foliation of Fe-Ti-rich and Mg-Al-rich metagabbro clasts, cemented by unfoliated eclogitic matrices (paragenesis: omphacite ± garnet ± lawsonite), demonstrates pristine brecciation at eclogite-facies conditions. Successive generations of high-pressure veins and eclogitic matrices reveal multiple brittle rupture events.

Pseudosection modeling, textural observations, and geochemical data suggest that minerals of both prograde veins and first brecciation event (M1 matrix) crystallized in presence of fluids buffered by the surrounding metagabbro minerals, while M2 matrix composition suggests an incipient infiltration of external fluids. Trace element composition of the third M3 matrix, associated to its impressive lawsonite pseudomorphs, clearly points to the massive ingression of external, serpentinite-derived fluids. Therefore, these rocks record the progressive increase in the scale of fluid circulation along multiple, stepwise eclogitic brecciation events, from locally released fluids (closed system) to kilometer-scale fluid infiltration. The successive brecciation steps promoted permeability creation (at least transiently), which resulted in progressive opening of the system to large-scale sustained fluid circulation. Eclogite-facies brecciation also controlled the initial stages of strain localization, which highlights the importance, in ductilely deforming low-permeability eclogite-facies rocks, of brittle deformation events for both strain localization initiation and creation of large-scale fluid circulation pathways. Thus, Monviso breccia blocks record the complete, stepwise development of a major shear zone, via progressive strain localization, permeability creation, and increasing scale of fluid circulation.

1. Introduction

Fluid release and transport in subduction zones has major consequences on both mass transfer and rheology. Fluids released by successive metamorphic dehydration reactions are crucial for mantle-wedge melting and arc magma genesis (e.g., Codillo et al., 2018; Defant & Drummond, 1990; Peacock, 1993; Schmidt & Poli, 1998; Stern, 2002; Figure 1a) and are commonly invoked as the main trigger for intermediate-depth, intra-slab earthquakes (e.g., Brudzinski et al., 2007; Fumagalli & Poli, 2004; Hacker et al., 2003; Hacker et al., 2003; Yamasaki & Seno, 2003). Fluid migration from the dehydrating slab toward the mantle wedge (e.g., Konrad-Schmolke et al., 2011; Kostenko et al., 2002; Marschall & Schumacher, 2012; Rupke, 2004) as well as the attenuation of seismic velocities (detected both in the wedge and in the slab; e.g., Nakajima et al., 2013; Shiina et al., 2013) imply large-scale fluid production and migration at intermediate depths (>50 km). But while the main lithologies contributing to aqueous-fluid release at these depths are well known (oceanic crust, serpentinite and, to a lesser volumetric extent, metasediments; e.g., Fumagalli & Poli, 2004; Hacker, 2008; van Keken et al., 2011), processes and pathways remain debated (e.g. Audet et al., 2009; Connolly, 2010; Davies, 1999; Zack & John, 2007). Eclogite-facies rocks are characterized by very low permeabilities (Brace, 1984; Watson & Brenan, 1987; Mibe et al., 2003; Morrow et al., 1984), which seem to restrict fluid circulation to fractures forming transient, short-lived fluid conduits (e.g., Bucholz & Ague, 2010; Glodny et al., 2003; Hermann et al., 2006; John et al., 2012; Penniston-Dorland et al., 2010; Philippot & Selverstone, 1991; Scambelluri & Philippot, 2001; Spandler & Hermann, 2006) and probably longer-lived high-strain zones channelizing fluids (e.g., Angiboust et al., 2014; Austrheim, 1987; Bebout & Barton, 1993; Konrad-Schmolke et al., 2011; Scambelluri et al., 2014).



Fluid circulation also triggers strain localization through mineralogical and associated rheological changes (e.g., strain weakening; e.g., Mancktelow & Pennacchioni, 2005; Wassmann & Stöckhert, 2013) and/or high fluid pressure-induced brittle deformation (e.g., Lund & Austrheim, 2003; Philippot & Selverstone, 1991). Several studies evidenced the key role of brittle precursors on strain localization and shear zone development (Angiboust et al., 2017; Hertgen et al., 2017; Locatelli et al., 2018; Mancktelow & Pennacchioni, 2005; Pennacchioni & Mancktelow, 2007), but the exact role of fluids on such transient switches between ductile and brittle deformation has remained unclear. For example, it is the presence of fluids triggering or resulting from brittle deformation (e.g., Hertgen et al., 2017; Locatelli et al., 2018; Pennacchioni & Cesare, 1997). If dehydration reactions with positive reaction volumes are considered as a potential trigger for brittle deformation associated to earthquake nucleation at the scale of subduction zones (e.g., Abers et al., 2013; Lund & Austrheim, 2003; Spinelli & Wang, 2009; Wong et al., 1997), small scale evidence is still debated, as shown by experimental data (i.e., dehydration embrittlement vs. transformational faulting; e.g., Incel et al., 2019, 2017; Okazaki & Hirth, 2016). Brittle precursors are likely erased by subsequent reworking, and examples of eclogite-facies brittle structures, such as high-pressure veins (Gao et al., 2007; John & Schenk, 2006; Philippot, 1987; Philippot & Kienast, 1989a; Widmer & Thompson, 2001) and eclogite-facies breccias (Angiboust, Langdon, et al., 2012; Angiboust, Agard, et al., 2012; Locatelli et al., 2018), are scarce.

In order to better document the complex interplay between brittle deformation, fluid circulation, and strain localization during subduction (e.g., Agard et al., 2018) and its role on the development of high-strain zones and associated fluid migration along/across slabs, we present a detailed (micro)structural and geochemical study of the successive brittle structures (i.e., high pressure veins and breccia matrices) found in the Western Alpine Monviso meta-ophiolitic belt. There, meter-scale eclogitic breccia blocks embedded in a serpentinite-rich matrix (Angiboust, Langdon, et al., 2012, Angiboust et al., 2011; Locatelli et al., 2019, 2018; Figures 1b–1e) crop out along >10-km-long shear zones and record several episodes of large-scale brittle deformation occurring near peak burial and at strong rheological contrasts (Locatelli et al., 2018).

The present study shows how these rocks constrain (1) the evolution of fluid sources and their migration scale during the stepwise evolution of the Lower Shear Zone (LSZ) and Intermediate Shear Zone (ISZ), (2) the implication of fluids in eclogitic brecciation, and (3) the mechanisms triggering the switch from ductile to brittle deformation observed in the Monviso metagabbros at eclogitic peak P–T conditions.

2. Geological Setting and Previous Works

The Monviso metaophiolite belt represents a well-preserved, 35-km-long and 8-km-large fragment of Tethyan oceanic lithosphere (Figure 1b), tectonically sandwiched between the UHP Dora Maira continental unit to the East and the sediments of Queyras Unit (Schistes Lustrés) to the West (e.g., Agard et al., 2002; Agard et al., 2009; Marthaler & Stampfli, 1989; Plunder et al., 2013). It used to be subdivided into six tectonometamorphic units (Lombardo, 1978) until the work of Angiboust, Langdon, et al. (2012), Angiboust et al., 2011), who suggested that the Monviso ophiolite is rather formed by two main coherent tectono-metamorphic units: the Monviso s.s. unit (MU; with peak P–T conditions at approximately 480 °C/22 kbar) overturned over the Lago Superiore Unit (LSU) (Figures 1b–1e).

This study focuses mainly on the LSU (Figures 1b–1e), which comprises, from bottom to top: a serpentinitized lherzolite sole, intruded and/or capped by late Jurassic Mg-Al metagabbros and minor Fe-Ti gabbros mostly at their top (or as centimeter- to meter-thick boudins intruding the primary oceanic lithostratigraphic sequence; e.g., Locatelli et al., 2019, 2018; Lombardo, 1978), banded tholeiitic basalts, and diabases and mixed calcareous/pelitic Cretaceous metasediments (Balestro et al., 2014, 2013; Castelli et al., 2002; Festa et al., 2015; Locatelli et al., 2019; Lombardo, 1978).

Eclogitic P–T peak conditions reported in literature vary for this unit: 580 °C/19 kbar (Schwartz et al., 2000), 650 °C/26 kbar (Messiga et al., 1999), 545 °C/20 kbar (Castelli et al., 2002), 550 °C/25 kbar (C. Groppo & Castelli, 2010, 2010), and 550 °C/26 kbar (Angiboust, Langdon, et al., 2012), 580 °C/28 kbar (Locatelli et al., 2018). Partial (but restricted) blueschist- and greenschist-facies overprint affected both the MU and the LSU during exhumation (e.g., Lardeaux et al., 1987; Locatelli et al., 2019; Schwartz et al., 2000).

The original stratigraphic sequence of the LSU is partly disrupted by two regional shear zones (Angiboust et al., 2011; Angiboust, Langdon, et al., 2012; Festa et al., 2015; Lombardo, 1978; Philippot & Kienast,

1989b): the ISZ localized between the metagabbros and the overlying metabasalts and the LSZ between the serpentinitized sole and the metagabbros (Figures 1b and 1e). The omphacite- and garnet-rich veins emplaced in metagabbros at the base of the ISZ (Lago Superiore area; Figures 1b and 1c) have been the subject of structural and petrological (Philippot, 1987; Philippot & Kienast, 1989a; Philippot & van Roermund, 1992), fluid inclusion (Nadeau et al., 1993; Philippot & Selverstone, 1991), stable isotope (Nadeau et al., 1993), geochronological (Rubatto & Hermann, 2003), and geochemical studies (Philippot & Selverstone, 1991; Rubatto & Hermann, 2003; Spandler et al., 2011). General consensus was reached by these works about the opening of the veins during prograde *ductile deformation* at high pressure and mineral crystallization in presence of locally derived hydrous fluid, then followed by ingress of external, potentially serpentine-derived fluids. Nevertheless, all these studies focused on a relatively restricted area (e.g., $\sim 1 \text{ km}^2$; Figures 1b and 1c) and lack representativeness for the entire portion of the subducted slab.

The recent report of *eclogite-facies breccias* in the LSZ (Angiboust et al., 2011; Angiboust, Langdon, et al., 2012; Locatelli et al., 2018), and subordinately in the ISZ too (Locatelli et al., 2018), have paved the way for investigating switches between ductile and brittle deformation at eclogite-facies depths.

In the LSZ, the largest part of the eclogite-facies breccias crops out as blocks disseminated in the antigorite-rich matrix of the shear zones (Figures 1b–1d). In the LSZ, three types of eclogitic blocks can be distinguished (Locatelli et al., 2019, 2018): (1) meter-sized blocks of brecciated Fe-Ti-metagabbros, scattered in the upper to intermediate levels of the LSZ (Type1 blocks; Figure 2a); (2) meter-sized blocks and decameter-scale slivers of intact Mg-Al metagabbros with eclogitic breccia layers crosscutting the preexisting eclogite-facies mylonite (Type2 blocks; Figures 2b and 2c), always localized on Fe-Ti metagabbro boudins inside the Mg-Al metagabbros; Type 2 blocks are also restricted to the upper to intermediate levels of the LSZ; (3) decimeter- to meter-scale blocks of intact, eclogite-facies Fe-Ti metagabbros without breccia fabrics (Type 3 blocks), restricted to the lower part of the shear zone, and interpreted as gabbro pods intruded in the serpentinite sole. Compared to the LSZ, only rare blocks of eclogitic metagabbro (corresponding to Type 2 blocks) crop out in the ISZ, chiefly on the western side of Lago Superiore (Locatelli et al., 2019, 2018; Figure 1c). On the eastern side of the lake, discontinuous, decimeter-thick breccia layers are found atop the Fe-Ti metagabbro boudins (Figure 1c) isolated from the surrounding antigorite schist of the ISZ by highly deformed Mg-Al metagabbros (comparable to the eclogitic brecciated boudins east of Truc Bianco, LSZ).

Eclogitic brecciation preferentially affected the Fe-Ti metagabbros (Locatelli et al., 2018, 2019), suggesting that rheological contrasts controlled the locus of brecciation. Here the variably rotated foliation of Fe-Ti-rich (omphacite + garnet + rutile \pm quartz \pm lawsonite and rare glaucophane) and scarcer Mg-Al-rich metagabbro clasts (omphacite + rutile \pm quartz \pm glaucophane \pm clinozoisite and locally garnet) cemented by unfoliated omphacite \pm garnet \pm lawsonite matrices demonstrate pristine brecciation at eclogite-facies conditions (see Locatelli et al., 2018, for further details). The occurrence of three generations of HP veins (paragenesis: omphacite \pm garnet \pm apatite similar to those described above for the Lago Superiore area) and a first omphacite-rich matrix M1 (crystallized at peak conditions; i.e., $\sim 2.7 \text{ GPa}$ – $580 \text{ }^\circ\text{C}$) cut by a second matrix M2 (omphacite + garnet; $\sim 2.4 \text{ GPa}$ – $560 \text{ }^\circ\text{C}$), itself reworked as clasts in a third matrix (M3), reveals multiple brittle rupture events. Massive fluid ingress during the last brecciation stage is witnessed by the crystallization of the lawsonite-rich matrix M3 (Locatelli et al., 2018). Late-stage metasomatism then affected the metagabbro brecciated blocks once disseminated in the LSZ serpentinite-rich matrix (Angiboust et al., 2014; Locatelli et al., 2018).

3. Deformation Stages and Samples

The complex history of progressive deformation during prograde subduction and eclogitic peak brecciation is schematically presented in Figure 2d. This offers the framework into which our samples of eclogitic breccias, veins, and adjacent host-rocks from both the LSZ and ISZ are placed (Figures 1b–1e). Importantly, all analyzed blocks (and brecciated Fe-Ti boudins) turned out to be very comparable; they overall document the same evolution with variably developed records of the different stages (in terms of macroscale or microscale structural characteristics). Detailed documentation of combined microstructural, petrographic, and geochemical data is presented in Table SM1.

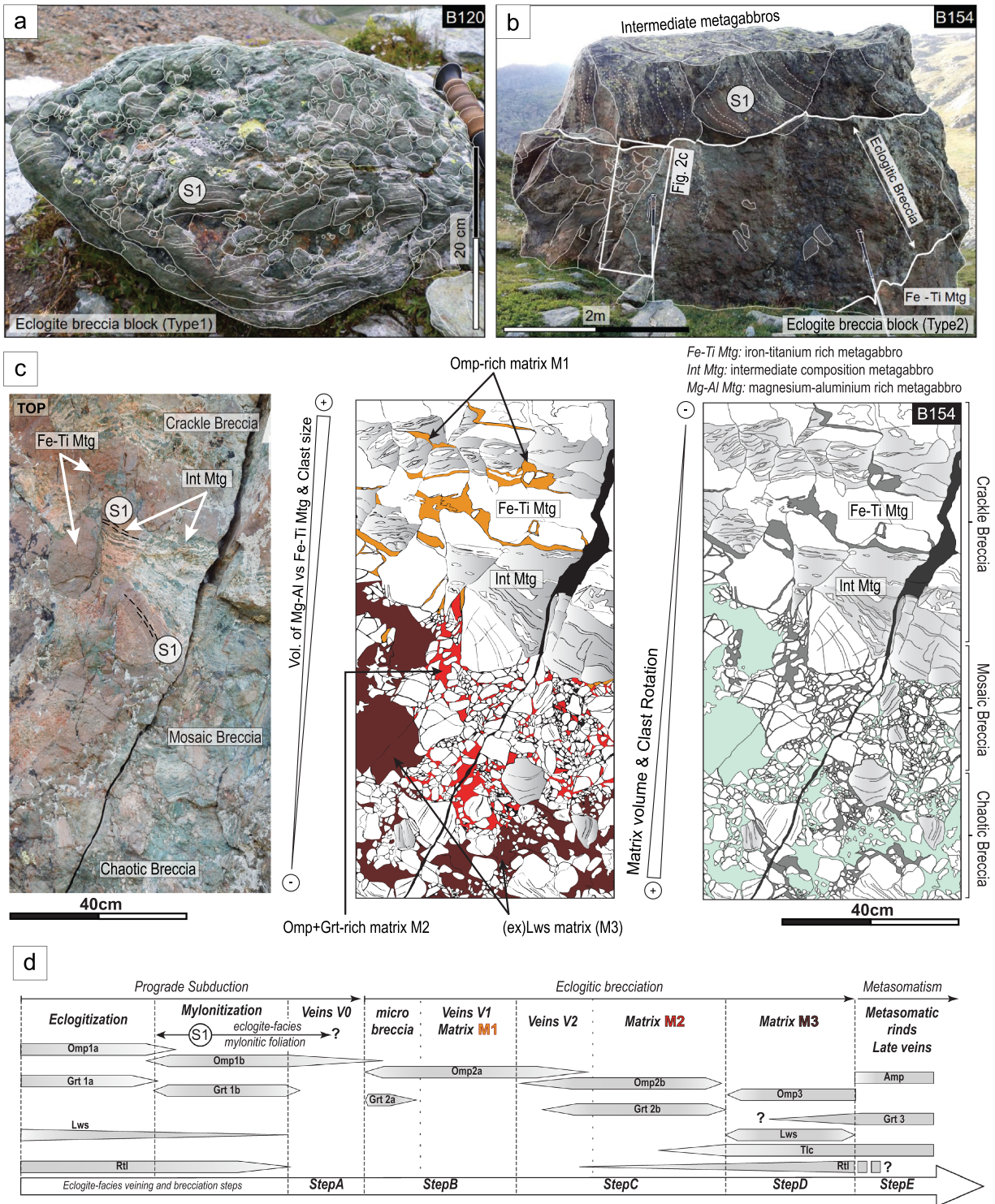


Figure 2. Eclogite-facies brecciated blocks. A exposure of a typical eclogite-breccia block (type 1). The clast-in-matrix structure with foliated Fe-Ti metagabbro overgrown by eclogite-facies matrix (here, the omphacite-rich M1 matrix) is well preserved under the pervasive lichen cover. Block from the upper Bulé Valley, NE of Colle di Luca pass. B example of the structures developed inside a type 2 block, with the eclogite-facies breccia crosscutting (here clearly subperpendicular) the folded, eclogite-facies S1 foliation of the intact mg-rich metagabbro. The breccia plane developed mainly on a Fe-Ti metagabbro boudin (former sill or dyke) inside the mg-rich metagabbro. Block B154, Pra Fiorito valley. C detail of a fully preserved, eclogite-breccia fault plane from block B63 with the transition from crackle breccia (at the top) to chaotic breccia (at the core). Used color code: White, Fe-Ti metagabbro clast; light-gray, mg-rich metagabbro clasts; orange, M1 matrix; red, M2 matrix; dark red, M3 matrix. D summary of deformation stages, paragenesis and mineral occurrence in eclogite-facies breccia. The “Steps A to D” at the bottom refer to the chronological evolution of brecciation and fluid circulation discussed in this paper and in Figures 11–13. Mtg = metagabbro.

3.1. Outcrop Scale: Structural Patterns of Eclogitic Breccia-Bearing Blocks

All the studied breccias from the LSZ were sampled from blocks completely enclosed within the antigorite schists of the shear zone (e.g., Figure 1b), except for those developed in the Fe-Ti metagabbro boudin outcropping W of Punta Forcion (samples *L63–15b* and *L63–15d*, east of Truc Bianco; Figure 1d), a boudin embedded in Mg-Al metagabbro that is situated in the lowest part of the Mg-Al gabbro cliff. Samples L14–10 and L14–11 crop out near the roof of the LSZ, east of the Rocce Sbiassere ridge. Blocks L20–15a and L20–15b and sample L73–15 were sampled on the northern flank of the Prà Fiorito valley, while samples L14–50 and L14–53 outcrop E of the Peiro Jauno ridge. It is noteworthy that all sampled blocks crop out near the roof of the LSZ (Figures 1b–1e).

Type 2 blocks from the LSZ exhibit the complete transition from intact metagabbros to breccia cores (Figures 2b and 2c): four Type 2 blocks were chosen among them to conduct a detailed structural and geochemical analysis (in Prà Fiorito valley, north of Alpetto Lake, and in the upper Bulè Valley; Figure 1b and Table SM1). On average, more than 80% of Type 2 blocks are formed by eclogite-facies, mylonitic Mg-Al metagabbro (paragenesis: omphacite + clinozoisite \pm ex-lawsonite and glaucophane, developing the S1 eclogite-facies foliation) and showing tight isoclinal folds (Figure 3a) locally embedding centimeter- to decimeter-scale boudins of Fe-Ti metagabbros (Figures 3a–3c). Fe-Ti metagabbros present the classical omphacite + garnet + rutile \pm lawsonite paragenesis and fabrics varying from massive to mylonitic. They are crosscut by a network of HP veins (e.g., omphacite bearing, which locally include host-rock fragments) up-to ~1-cm thick, developed almost perpendicular to the foliation in the thinnest boudins (e.g., thickness between ~2 and ~10 cm; Figure 3b) and with a radial arrangement in the biggest boudins. The opening geometries vary from crack seal to tension gashes, similar to geometries of veins crosscutting the Lago Superiore Fe-Ti metagabbros in the ISZ (Philippot & Selverstone, 1991; Spandler et al., 2011). Interestingly, these tapering veins developed in Fe-Ti metagabbros progressively disappear into the decimeter-thick layer of garnet-bearing Mg-Al metagabbros (*intermediate metagabbro*; hereafter; Figure 3c and Tables SM2a and SM2b) systematically observed at their contact, as these veins are sheared parallel to the eclogitic foliation of the Intermediate metagabbro, suggesting that shearing partly postdates vein formation (e.g., Locatelli et al., 2018). Both the eclogite-facies mylonitic foliation of Mg-Al metagabbro and the boudins of Fe-Ti metagabbro (as well as some of the HP veins) are sharply truncated, unconformably, by eclogite-breccia horizons (Figures 2b, 2c, and 3a). The complete transition, toward breccia cores, from intact rock to (I) crackle, (II) mosaic, and (III) chaotic breccia (*sensu* Sibson, 1977) is observed in fully preserved breccia planes (Locatelli et al., 2018). This progressive change in breccia fabrics is characterized by the increase in matrix content and angle of clast rotation from intact rock to chaotic breccia, with correlated comminution of clasts (which diameter decrease from decimeter to centimeter size; Figure 2c).

All the analyzed eclogitic breccia planes show a bimodal clast composition (Figures 2c and 3d–3f) with ~90% (modal amount) constituted by Fe-Ti metagabbro and rarer (~10%) Mg-rich metagabbros. The Mg-rich metagabbros in clasts show the same fabrics and composition than those constituting the bulk of *Type 2* blocks (e.g., Figures 2c and 3b), whereas the mylonitized Fe-Ti metagabbro clasts are comparable to the boudins embedded in *Type 2* blocks. In most cases, rotated clasts were cemented after brecciation by a succession of newly-formed, eclogite-facies matrices (Figures 3e and 3f).

3.2. Decimeter- to Millimeter-Scale Structures of Eclogitic Breccia Layers

3.2.1. Eclogite-Facies Matrices

The amount of matrix crystallizing in between the eclogitic breccia planes increases from rims to cores of breccia levels (e.g., Figure 2c); crosscutting and textural relationships allow distinguishing four successive matrix types (Figures 2c, 3a, and 3d–3f):

- I At the contact with intact rock (Figure 2c), inside the first 10 to 20 cm of brecciated layers, slightly rotated clasts are surrounded by anastomosed, submillimeter domains of finely comminuted grains (<100 μm) of Fe-Ti metagabbros (*microbreccia*; hereafter, *sensu* Locatelli et al., 2018).
- II Such domains are overgrown by small amounts of newly crystallized, light green omphacitic cement (*matrix M1*; hereafter, e.g., Figures 2c, 3d, and 3f), which amount increases (up to 1-cm-thick mantles around clasts; Figure 3d) while *microbreccia* progressively disappears toward breccia cores.
- III Both the *microbreccia* and the *matrix M1* are postdated by the crystallization of *matrix M2* (e.g., Figures 2c and 3f). This omphacite- and garnet-bearing matrix crystallizes around the clasts, forming

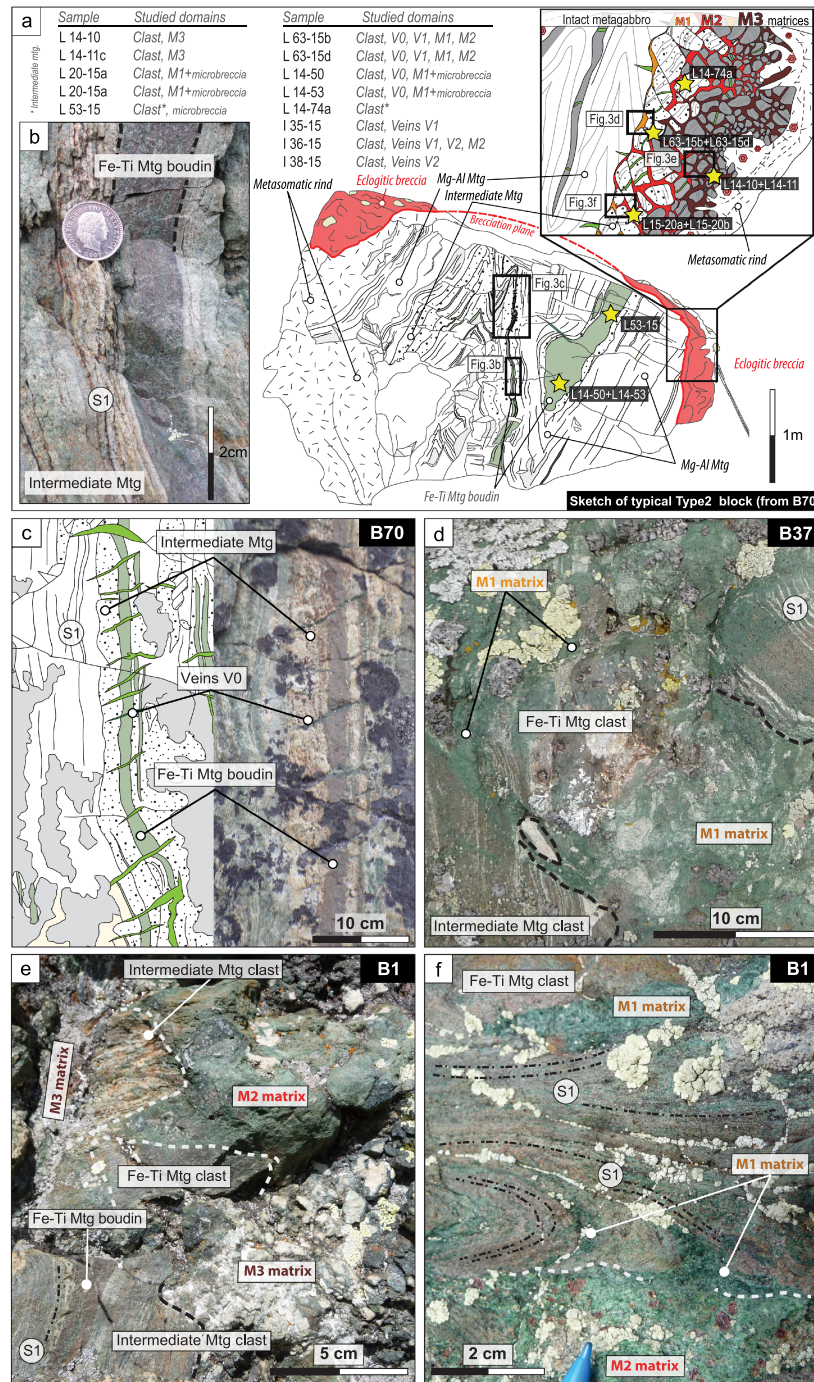


Figure 3. Chronology of successive matrix generations in breccia planes. A typical meter-scale type 2 block. The eclogitic breccia crosscuts (here at high angle) the preexisting mylonitic foliation of the intact mg-Al metagabbro. Note the complex folding of the Fe-Ti boudins in the intact metagabbro. The inset shows a schematic view of the typical structuration of eclogite-breccia layers, with progressive increase of clast comminution and rotation toward the breccia core (M3 matrix rich). The positions of samples depict their structural domain but are derived from different outcrops (see SM1). B close-up view of a centimeter-thick Fe-Ti metagabbro boudin embedded in intermediate metagabbro; brownish rutile ribbons sup-parallel to the boudin mark the eclogitic S1 foliation. Block 70, Prà Fiorito valley. C Omphacite (Omp) ± apatite (apt) bearing veins V0 crosscutting at high angle a Fe-Ti metagabbro boudin; note the tapering of the veins at the contact with the intermediate metagabbro. Block 70, Prà Fiorito Valley. D typical clast-in-matrix appearance of eclogite-facies breccia on fresh surface. Here the rotated metagabbro clasts are cemented by omphacite-rich matrix (M1). Veins in the clasts are filled by fibrous Omp ± apt. Block B37, NW of Alpetto. E Eclogitic metagabbro clasts (with obvious mylonitic foliations S1) sealed by crystallization of Lws-rich matrix M3. Noteworthy, in the upper-center part of the picture, the occurrence of a clast composed by reworked eclogite-facies breccia (mylonitic metagabbro clasts cemented by Omp-rich matrix M1). Block B45, south of Punta Murel. F Eclogitic Fe-Ti metagabbro (with folded mylonitic foliations S1) overgrown by Omp-rich M1 matrix. Note, in the lower part of the picture, the occurrence of Omp + Grt bearing M2 matrix, sharply crosscutting all the previous structures. Block B1, NW of Alpetto.

mantles up to 3-cm thick and, in hand-specimen, is well recognizable by the bigger size of garnets with respect to mylonitic Fe-Ti clast garnets (Figure 3f).

- IV In the core of brecciated layers (i.e., *chaotic breccia fabrics*—Figure 2c; refer also to Locatelli et al., 2018), crosscutting relationships show that a late matrix M3 postdates both matrices M1 and M2 (e.g., Figure 3e). M3 shows penetrative fracturing at the core of breccia layers (Figure 2c) and is the most abundant matrix type. In fact, numerous clasts are composed by mylonitic metagabbro \pm M1 \pm M2 matrices cemented by newly formed M3 (Figure 3e), suggesting that M3 emplacement was driven by hydraulic fracturing of pre-existing breccia. M3 is characterized by impressive euhedral lozenge-shaped pseudomorphs after lawsonite (<2 cm; Figure 3e), accompanied by relics of *omphacite*, *talc* and *chlorite* \pm *rutile* aggregates after garnet.

It is important to note that all these matrices show only minor evidence of crystal-plastic deformation on omphacite (Omp2a/2b, Omp3; Figure 2d; sensu Locatelli et al., 2018) while the clasts always show a strong mylonitic foliation (Omp1a/1b, Figure 2d; sensu Locatelli et al., 2018).

3.2.2. Eclogite-Facies Veins

Two successive sets of submillimeter scale veins are found in the clasts of the LSZ: *Veins V0* (omphacite bearing) and *Veins V1* (omphacite \pm apatite bearing). Veins V0 are generally subparallel to the mylonitic foliation of clasts (e.g., Figures 4a–4e), while Veins V1 formed both as massive, irregular-shaped veins with euhedral crystals or as syntaxial veins (thickness up to 2 cm) with acicular omphacite crystals (Figure 4a), cutting the metagabbros fabrics at variable angles (e.g., Figures 4a and 4b). Both sets are postdated by the crystallization of M1 or (locally) M2 matrices (e.g., Figures 2c, 4a, and 4b). In the ISZ, an additional vein set is observed: *Veins V2* (omphacite + garnet bearing), postdating both Veins V0 and V1 (e.g., Figure 4d). All these structures are cut across by the M2 matrix (e.g., Figure 4a).

In the LSZ, a later stage set of veins (hereafter *Late-stage veins*), filled with talc, clinopyroxene, and subordinate chlorite, sharply crosscuts both clasts and all matrices (e.g., Figure SM2c) and, thus, postdates the brecciation events.

3.2.3. Metasomatic Rinds

In the LSZ, at the contact with the antigorite-rich matrix embedding them, brecciated blocks are rimmed by a hydrated metasomatic rind that can locally reach 0.5-m thickness (e.g., in Lago Superiore, Pta. Forcion, and Colle di Luca). This metasomatic replacement affects clasts, matrices, and Late-stage veins (Figures 4c–4e and SM3a) and, thus, postdates their formation. Here a complex set of submillimeter scale veins filled with hydrous minerals nucleates from the metasomatic rinds and radially crosscuts the surrounding clasts as well as M1 and M2 domains (e.g., Figure 4c).

3.2.4. Notable Differences Between the LSZ and the ISZ

Compared to other eclogitic blocks in the LSZ, the eclogite breccias from the Fe-Ti metagabbro boudin at the base of the Truc Bianco peak (Figures 1c and 1e) shows similar structures (i.e., clasts locally crosscut by veins and embedded in matrix; Locatelli et al., 2018) but without M3 lawsonite-rich matrix. Similarly, in the ISZ, all the breccia boudins (Figure 1c) also lack any evidence for M3 (e.g., Figures 4a and 4b), as well as M1, crystallization. Contrary to those found in the ISZ, veins V0 and V1 from the LSZ blocks can be locally sheared and/or folded inside the mylonitic foliation of clasts and the host rock (e.g., Figure 3e and Table SM3b).

4. Analytical Techniques

4.1. Bulk-Rock Geochemical Analysis

Twenty-seven fist-sized samples of eclogite-facies matrices, eclogitic Fe-Ti and Mg-Al metagabbro (host rock), metasomatic rinds, veins V1 and V2, and LSZ serpentinite from the Lago Superiore Unit (Table SM1) were crushed in a steel jaw crusher and then milled to fine powder in an agate mill. A small amount of crushed, inclusion-free hydrothermal quartz was milled between each sample to prevent cross contamination. Additionally, a small amount of the rock intended to be milled was crushed for 10 min, to self-contaminate the mill and fade the signals of precedent samples. Bulk rock chemical analyses were performed at the SARM-CRPG (Nancy, France) and at EOST (Strasbourg University, France). Major elements were analyzed by inductively coupled plasma (ICP)-optical emission spectroscopy after fusion with LiBO₃ and dissolution in HNO₃. Trace elements were quantified by inductively coupled plasma mass spectrometry (ICP-MS) following the procedure described by Carignan et al. (2001).

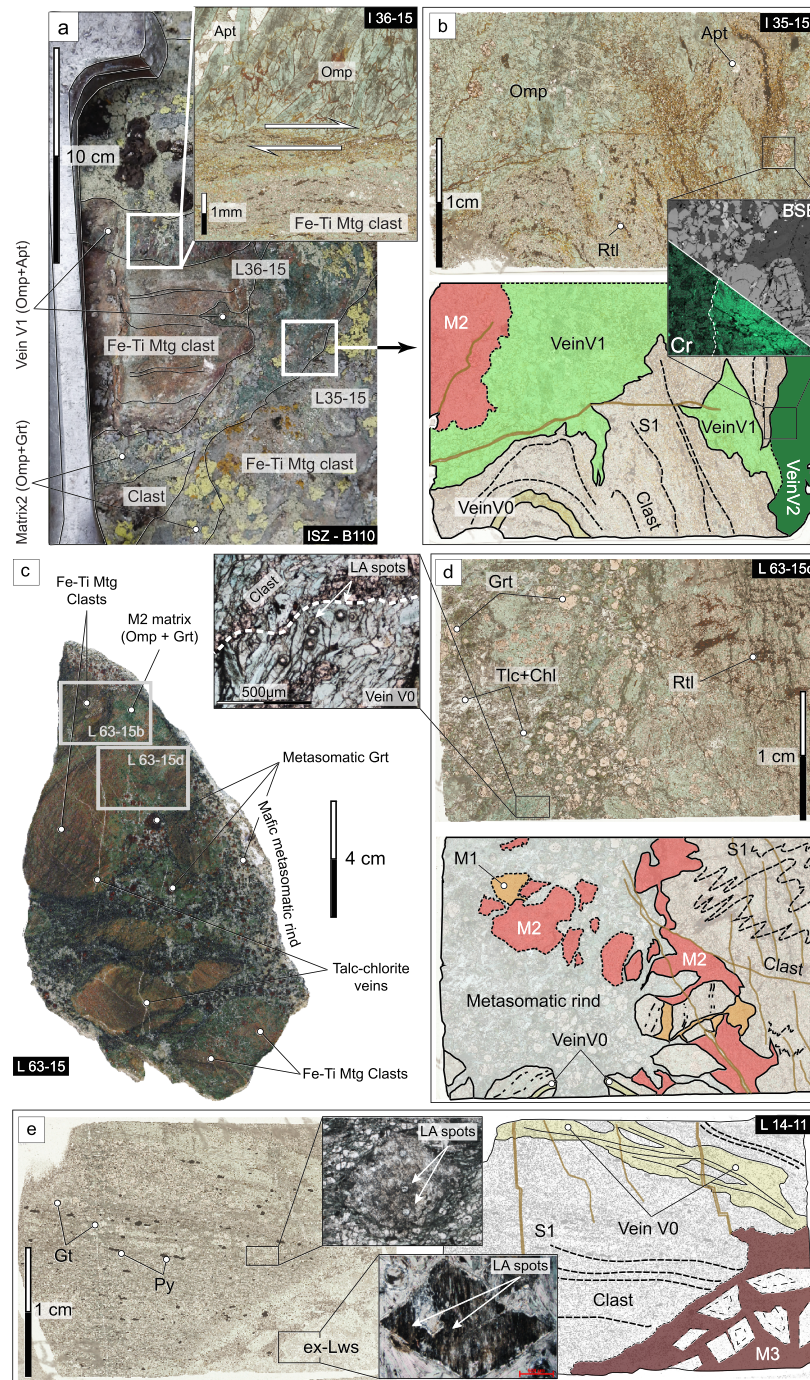


Figure 4. Brecciated eclogites at meso- to thin-section scale. A photo of a breccia sample from the ISZ, with M2-matrix (omphacite (Omp) + garnet (Grt)) cementing clasts of Fe-Ti metagabbro hosting fibrous vein V1 (detail in the inset). B scan of sample I35-15 (ISZ), summing up the microstructural relationship between mylonitic clast, veins and matrix M2; in the inset, a SEM map showing the different Cr concentration between garnet from M2 matrix (enriched) and the atoll garnets from the mylonitic clast. Sample from block B110, W of Lago Superiore. C polished slab of eclogite breccia documenting the crosscutting relationships between mylonitic clasts, the matrix M2 (Omp + Grt) and the metasomatic mineralization (talc (Tlc) + chlorite (Chl) + Grt + amphibole (amp) ± ca-rich diopside). The darker areas (mainly developed in the matrix portions) are Chl/Amph-rich recrystallization linked to late-stage retrogression under green-schist facies condition. Shown are the positions of samples L63-15b and L63-15d. Sample from the base of Truc Bianco cliff. D photograph of a thin section across mylonitic, eclogite-facies Fe-Ti metagabbro and a matrix domain. Note the complex succession M1-M2 matrices, with the pervasive, late-stage metasomatization developed only at the expenses of matrices. The inset shows a detail of the fibrous Omp ± apt (apatite) crystals of veins V0; the holes are from laser ablation measurements. Sample L63-15d. E photograph of a thin-section across mylonitic, lawsonite (Lws) bearing Fe-Ti metagabbros overgrown by M3 matrix. The boxes illustrate the lawsonite crystals (now pseudomorphosed by epidote + phengite ± plagioclase) with laser ablation holes. Sample L14-11. Rtl: Rutile; Py: Pyrite. Thin-section photos in a-e: Plane polarized light.

4.2. X-Ray Mapping and Mineral Major Element Analysis

The microstructures of the 12 analyzed samples were studied at the thin section scale using both optical microscope and SEM (Zeiss Supra 55VP, associated to SSD detector PTG Sahara for EDS analysis; *ISTeP, SU, Paris*).

Electron Probe Micro-Analyzer (EPMA) measurements (CAMECA FIVE and SX100) were performed at CAMPARIS (*ISTeP, SU, Paris*). Major element measurements on clinopyroxene, garnet, rutile, apatite, chlorite, talc, epidote, plagioclase, phengite, and ex-lawsonite were performed using a 15 kV acceleration voltage and 10 nA beam current, wavelength-dispersive spectroscopy. Acquired data were processed using *j* (rZ) corrections and standardized against a set of well-characterized, in-lab standards: Fe₂O₃ (Fe), MnTiO₃ (Mn, Ti), diopside (Mg, Si), CaF₂ (F), orthoclase (Al, K), anorthite (Ca), albite (Na), and silicate (albite, almandine, forsterite, and wollastonite).

EPMA major element mapping of matrix and clast minerals was done using the CAMECA FIVE, using a beam at 15 kV acceleration voltage and 10 nA. The mapping was run by point scanning in steps of 2 μm, with dwell times set at 50 ms for Si, Ti, Al, Mg, Ca, Mn, Na, and K and at 300 ms for Cr and Ni. The Fe²⁺ and Fe³⁺ contents of clinopyroxene and garnet were calculated on the basis of charge balance, assuming perfect stoichiometry. All Fe was assumed to be Fe²⁺ in talc and Fe³⁺ in rutile.

4.3. Mineral Trace-Element Analysis

LA-ICP-MS measurements of vein and host-rock minerals were done at the *Institute of Geological Sciences, University of Bern, Switzerland*, using a Geolas Pro 193 nm ArF Excimer laser (Lambda Physik, Germany) coupled with an ELAN DRcE quadrupole mass spectrometer (Perkin Elmer, USA). Details on the setup and optimization strategies can be found in Pettke et al. (2012). Laser energy on sample surface was tuned to an ablation rate of approximately 0.15 μm per pulse. A custom-built 20-cm³ ablation cell was used, and the aerosol carrier gas was a He-H₂ mixture. The analytical setup was tuned daily for optimum performance across the entire mass range. External standardization was carried out using GSD 1G and NIST SRM 612 glasses.

Each signal was carefully evaluated during off-line data reduction using SILLS software (Guillong et al., 2008), with rigorous limits of detection calculated for each element in every analysis following the formulation detailed in Pettke et al. (2012). Integration intervals were set to avoid contributions from accidentally ablated inclusions and/or cracks. Internal standardization employed major element concentrations determined by EPMA for minerals, or the sum of measured major element oxides (i.e., 100 wt% minus stoichiometric H₂O content of 11 wt%) for the bulk reaction product composition of former lawsonite crystals.

5. Bulk-Rock Geochemistry

5.1. Metagabbros and Serpentinite

Mg-Al metagabbro samples from the LSU have mafic compositions, with low Fe₂O₃ (2.13–7.80 wt%), TiO₂ (0.25–0.86 wt%), Ni (162.09–201.57 μg/g), and Co (20–48 μg/g) contents relative to the mid-ocean ridge basalt (MORB; McDonough et al., 1996; Sun & McDonough, 1989; Figures 5a–5g). Chromium contents (Table 1 and Figures 5c and 5e–5g) vary between 350 and 563 μg/g in the LSZ Type2 blocks to a maximum of 2,590 μg/g in the eclogitic metagabbro cropping out E of Lago Superiore (ISZ; Table 1). In the latter sample, such Cr enrichment is related to the crystallization in the bulk of the rock of centimeter size, Cr-rich omphacite (kosmochlor). When compared to the eclogitic Fe-Ti metagabbros (Table 1 and below), the Mg-Al metagabbros are richer in MgO, Al₂O₃, CaO, Cr, Ni, and Sr (e.g., Figures 5a–5c) but have lower contents of FeO, TiO₂ and most incompatible elements (Figure 5c). These less fractionated compositions along with positive Eu anomalies that are not observed for the Fe-Ti metagabbros (Table 1 and Figure 5c) suggest a plagioclase-rich cumulate nature of the Mg-Al metagabbros.

The mylonitic, unbrecciated Fe-Ti metagabbro eclogites that crop out at the top of the Mg-Al metagabbros south of Lago Superiore (ISZ), have mafic compositions (Figures 5a and 5b) with high Fe₂O₃ (16.69–21.10 wt%) and TiO₂ (1.1–4.6 wt%) and low Cr (7.72–42 μg/g), Ni (22–60 μg/g), and Co (20–46 μg/g) contents relative to the MORB (McDonough et al., 1996; Sun & McDonough, 1989). These compositions are similar to the other Lago Superiore eclogites (Rubatto & Hermann, 2003; Schwartz et al., 2000; Spandler et al., 2011)

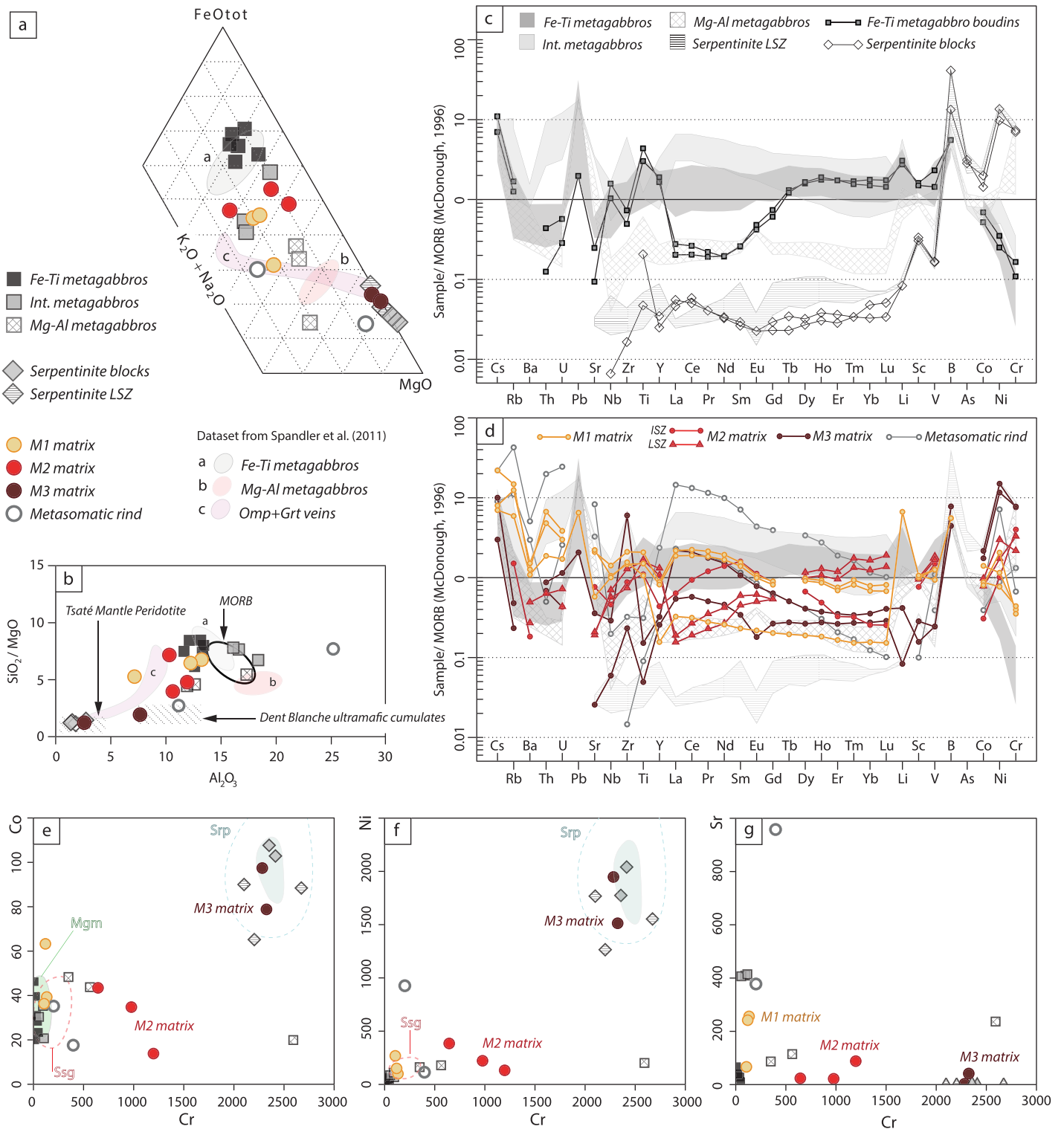


Figure 5. Bulk-rock chemical compositions of Monviso metagabbros, eclogite-facies breccia matrices and serpentinite. A FeO-MgO-(K₂O-Na₂O) and b SiO₂/MgO vs. Al₂O₃ (anhydrous wt%) diagrams of analyzed bulks; the fields of the data of Spandler et al. (2011) from the ISZ area are also plotted, for comparison purposes. Tsaté mantle and the dent Blanche ultramafic cumulates are added in (b) as external references and are from Manzotti et al. (2017). The MORB array is from Bodinier and Godard, 2003, and references therein. (c and d) trace elements variation diagrams for bulks of selected samples (table 1). The data are normalized to pyrolite values from McDonough and sun (1995). (e-g) Selected binary diagrams for bulk-rocks. Noteworthy the similar geochemical composition of M1 matrix bulk with respect to intermediate metagabbros; samples of M3-matrix and metasomatic rinds show affinity with serpentinite compositions. Ssg: Gabbro compilation from Indian Ocean (Bach et al., 2001); Mgm: Monviso metagabbros (Angiboust et al., 2014); Srp: Serpentinite compilation (Deschamps et al., 2013).

and compare well with more fractionated ferrobasalts of the oceanic crust (e.g., Bach et al., 2001; Carmichael, 1964; Wood, 1979).

The centimeter- to decimeter-thick, boudinaged Fe-Ti metagabbros locally embedded in Mg-Al metagabbros show comparable contents in Fe_2O_3 (16.69–19.76 wt%), Cr (32–50 $\mu\text{g/g}$), Ni (33–46 $\mu\text{g/g}$), and Co (23–31 $\mu\text{g/g}$) but higher TiO_2 (4.30–6.20 wt%) with respect to the Lago Superiore Fe-Ti metagabbros (Figures 5a and 5e–5g). Here the REE show a peculiar trend (Figure 5c), with light REE (LREE) concentrations similar to those of Mg-Al metagabbros and, in contrast, heavy REE (HREE) concentrations shifting toward those observed in Fe-Ti and Intermediate metagabbros (Table 1).

Intermediate metagabbros, found as centimeter-thick bands of garnet-bearing Mg-Al metagabbros at the transition with the Fe-Ti metagabbro boudins (i.e., surrounding them), show compositions in most major elements that are intermediate between Fe-Ti and Mg-Al metagabbros (Table 1 and Figures 5a and 5b). Their trace element composition is generally closer to that of Fe-Ti metagabbros (Figure 5c), although they are enriched in elements such as Cs, Rb, Ba, Th, U, Zr, as well as LREE, Ni, and Cr (Table 1 and Figures 5c and 5e–5g). However, they show lower concentrations in As, Co, Ni, and in particular Cr (1 to 2 orders of magnitude lower) than the surrounding Mg-Al metagabbros (Table 1 and Figure 5c).

Three serpentinites from the antigorite-rich schists of the LSZ and two from the massive blocks dispersed in the shear zone matrix were analyzed (Table 1 and Figures 5a–5c). Both the blocks and the serpentinites composing the bulk of LSZ matrix are largely harzburgitic and have compositions typical of hydration on the ocean floor, including high concentrations of B (12–37 $\mu\text{g/g}$), As (1.3–2.2 $\mu\text{g/g}$), and Sb (0.064–0.11 $\mu\text{g/g}$) along with high MgO, Cr, Ni, and LOI relative to typical mantle peridotite (Table 1 and Figure 5c). These data are consistent with the Monviso serpentinite data of Hattori and Guillot (2007), Spandler et al. (2011), and Angiboust et al. (2014).

5.2. Eclogite-Facies Matrices

The bulk major element composition of M1 matrix (Table 1 and Figures 5a, 5b, and 5d) reflects the high modal abundance of omphacite, often exceeding 95 vol.%. Trace element patterns largely correspond to those of Fe-Ti and Intermediate metagabbros. Precisely, M1 matrices are enriched in Rb, Th, U, Li, and B but also Cr (106–132 $\mu\text{g/g}$), Ni (100–268 $\mu\text{g/g}$), and less so for Co (36–63 $\mu\text{g/g}$; Table 1 and Figures 5d–5g) and depleted in Y compared to Fe-Ti metagabbros, with concentrations comparable to those of Intermediate metagabbros (Table 1 and Figure 5d). REE patterns are similar to those of intermediate metagabbros (i.e., decreasing from LREE to HREE), although showing lower concentrations, in particular in LREE (concentrations similar to those of Fe-Ti metagabbros; Figure 5d).

Samples of M2 matrix show concentrations in large ion lithophile elements (LILEs), Nb, Zr, Ti, Y, Sc, V, and Co close to those of Fe-Ti metagabbros, that is, lower than in M1 matrix (Figure 5d). On the contrary, Cr and Ni are enriched in M2 matrix compared to surrounding Fe-Ti metagabbro clasts, their Cr contents being in the range of those of Mg-Al metagabbro (Table 1 and Figures 5d–5g). MORB-normalized REE patterns strongly differ for M2 matrix depending on location (Figure 5d): M2 from the ISZ shows hump-shaped REE spectra with higher LREE and lower HREE concentrations compared to LSZ M2 samples, which show REE concentrations decreasing from HREE to LREE.

M3 matrix has lower contents of TiO_2 (0.07 w-%), Fe_2O_3 (8.96 wt%), and CaO (1.48 wt%) than both Mg-Al and Fe-Ti metagabbros, but MgO (33.97 wt%) is strongly enriched with respect to all the other lithologies (Table 1 and Figures 5a and 5b). Contents of both major and some trace elements are comparable to those of the analyzed serpentinite samples: high contents in Cr (2,280–2,330 $\mu\text{g/g}$), Ni (1,510–1,950 $\mu\text{g/g}$), Co (79–97 $\mu\text{g/g}$), and B (4–7 $\mu\text{g/g}$) (Table 1 and Figures 5a, 5b, and 5d–5g), as well as depleted concentrations in Li, Sc, V, and Sr (Table 1 and Figure 5d). To the contrary, the REE patterns (high LREE vs. HREE) do not compare well to those of serpentinites, metagabbros, or other matrices (Figure 5d), while most of the LILE concentrations are comparatively low (often below their detection limits; Table 1 and Figure 5d).

6. Textures Versus Major Element Mineral Chemistry

The SEM and EPMA analyses suggest that the major element compositions of mylonitic clinopyroxene and garnet (Tables 2 and 3 and Figures 6a and 6b) present only minor differences between Mg-Al and Fe-Ti

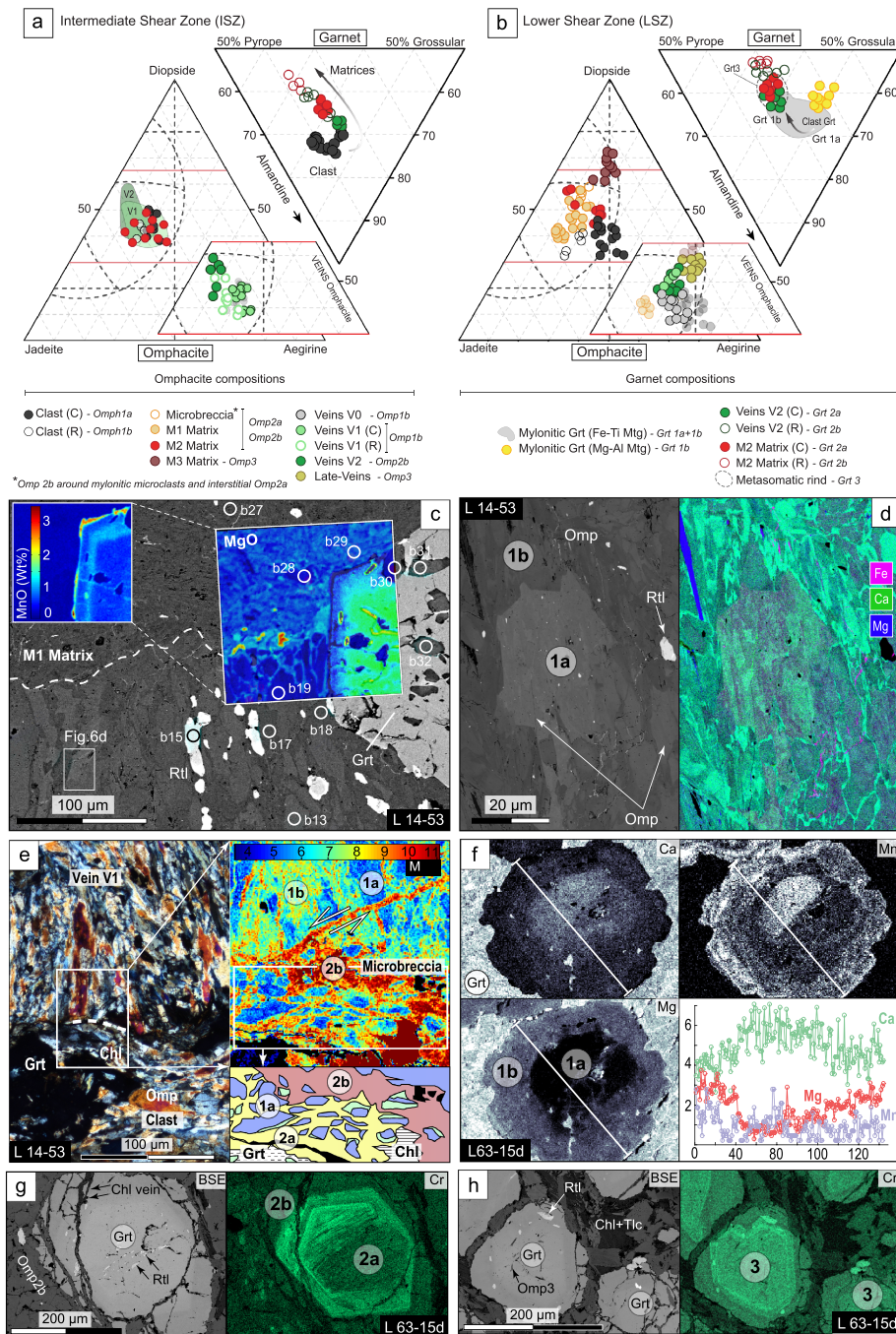


Figure 6. Major element compositions and chemical maps of omphacite and garnets. (a and b) major element composition of minerals (EPMA data) then analyzed by LA-ICP-MS for samples from (a) ISZ and (b) LSZ. Ternary plots are for omphacite (jadeite-diopside-aegirine) and garnet (grossular-almandine-pyrope). (c) BSE-SEM image of the complex zonation of omphacite crystals at the transition from mylonitic clast to M1-matrix domains. The box to the right illustrates the quantified EPMA map for MgO that highlights the strong compositional variation between mylonitic *Omp1a* and *Omp1b* (dark blue) with respect to the *Omp2a* (light blue); the latter, from the matrix domain, infiltrates and seals the mylonitic crystals at the clast border only. The box to the left displays the EPMA map of MnO, showing its strong enrichment in the garnet rims at the contact with M1-matrix. Sample L14-53. (d) BSE-SEM image of the complex zonation of omphacite crystals developed in mylonitic Fe-Ti metagabbro clasts; to the right the FEG-SEM quantified Ca (green), Fe (pink), and Mg (blue) map of the same area. Sample L14-53. (e) Cross-polarized light microphotography of a microbreccia domain developed between a mylonitic metagabbro clast (lower part of the figure) and an *Omp* + apt-bearing vein V1 (upper part of the figure). The quantified EPMA map of MgO shows the “infiltration” pattern of the MgO-rich *Omp2b*. Sample L14-53. (f) FEG-SEM quantified maps of a garnet from a mylonitic Fe-Ti metagabbro clast. Sample LSZ 63-15d. (g) FEG-SEM quantified maps of a garnet from M2 matrix. Note that the Cr zonation of garnet shows an oscillatory, dissymmetric pattern which has no equivalent in mylonitic and metasomatic garnet. Sample L63-15d. (h) FEG-SEM quantified maps of a garnet from a metasomatized portion of sample L63-15d. Chromium is strongly enriched and, differently from M2 garnet, shows a symmetric zonation. Mineral abbreviations as in Figure 4.

metagabbro clasts. Similarly, the major element compositions of matrices M1, M2, and M3 do not show any striking difference between the different samples, so the data are presented together in the following. The representative major element compositions for omphacite, garnet, ex-lawsonite, and apatite are presented in Tables 2–5. The full set of major element data of minerals is presented in Table SM5.

6.1. Clast Minerals (in the LSZ)

In the clasts, omphacite crystals (Figures 6a and 6b) show clear core-to-rim chronological relationships (e.g., Omp1a and Omp1b sensu Locatelli et al., 2018). In the mylonitic Fe-Ti metagabbro clasts, the first generation of omphacite (Omp1a, $\text{Di}_{45}\text{Jd}_{30}\text{Aeg}_{25}$; Figures 6a–6e) forms bright porphyroclasts (Figures 6c and 6d), rimmed by a second omphacite generation (Omp1b, $\text{Di}_{40}\text{Jd}_{38}\text{Aeg}_{22}$; Figures 6a and 6b) crystallizing also as newly formed crystals aligned in the mylonitic foliation. Garnet is also zoned (Figures 6a and 6b), with dark-colored cores (Grt1a, $\text{Grs}_{24}\text{Prp}_{5}\text{Alm}_{71}$; Tables SM3c and SM3d) and lighter rims (Grt1b, $\text{Grs}_{17}\text{Prp}_{13}\text{Alm}_{70}$; Tables). Interestingly, garnet cores (Grt1a) have numerous Omp1a inclusions, whereas the rims (Grt1b) only contain few inclusions of Omp1b, showing that omphacite and garnet compositions evolved jointly during mylonitization. Locally, garnets with smaller size ($<100\ \mu\text{m}$) of Grt1b composition are scattered in the foliation (SM3c and SM3d). Veins V0 (i.e., folded along the mylonitic foliation; Figures 4a and 5b) and Veins V1 (i.e., cutting across the clasts mylonite) are filled with unzoned Omp1b crystals and subordinate apatite.

6.2. Matrix and Rind Minerals (in the LSZ)

Fragmented omphacite and garnet crystals compose the bulk of the microbreccia domains (Figure 6e), with compositions and zonations comparable to those of mylonitic clast minerals (i.e., Omp1a cores rimmed by Omp1b compositions and Grt1a rimmed by Grt1b). Interstitial Omp2a omphacite (Figure 6e) crystallizes around microbreccia grains (Figure 6e), and fragmented Grt1 garnets in contact with Omp2a layers are overgrown by thin ($<20\ \mu\text{m}$) Mn-rich mantles of Grt2a composition (see also Locatelli et al., 2018). Anastomosed layers of Omp2b ($<70\ \mu\text{m}$ thick), with infiltration-like pattern departing from M1 matrix domains, overgrow both interstitial Omp2a and the microbreccia domains (Figure 6e).

The zonation of omphacite crystals in M1 and M2 matrices is more complex than in clasts and microbreccia, with transitions difficult to unravel (e.g., Omp2a to Omp2b; Figures 6b and 6c). The M1 matrix (omphacite bearing) is composed of about 60 vol.% of Omp2b crystals surrounding flake-shaped remnants of corroded, Al-richer Omp2a crystals (35 vol.%, Figures 6b and 6c). The intergrowth of the two omphacites results in an extremely intricate mesh of both generations (e.g., MgO concentration of M1 matrix shown in Figures 6b and 6c), with rare remnant of comminuted Omp1a/b crystals and rutile (~ 5 vol.%). M2 matrix (omphacite and garnet bearing) is largely made of tabular omphacite crystals of Omp2b composition, with subordinate Omp2a (mainly as crystal cores) and rare Omp1a-b clast relics (Figure SM3c); composition of Omp2b is similar to the one analyzed in microbreccia and M1 matrix but noticeably enriched in Cr_2O_3 locally (up to 0.10 wt.% in the LSZ and 2.16 wt.% in the ISZ; Table 2 and complete database on SM5). Here garnet cores (Grt2a composition, Figure 6b) are rimmed by almandine-poorer garnet (Grt2b; $\text{Grs}_{20}\text{Prp}_{25}\text{Alm}_{45}$). Both are clearly enriched in Cr_2O_3 when compared to mylonitic clast Grt1 (maximum concentrations respectively up to 0.50 and 0.10 wt.%, Table 3 and complete database on SM5), with peculiar sectorial enrichment patterns (Figure 6g). In Grt2a, omphacite inclusions have Omp2a compositions, while Grt2b appears to be equilibrated with inclusions of Omp2b. Analysis of the M3 matrix eclogite-facies assemblage is difficult due to the strong greenschist retrogression (Figures 4e and SM3e and SM3f), which lead to pervasive recrystallization of tremolite/actinolite + plagioclase after omphacite and chlorite \pm phengite after garnet (as described in Locatelli et al., 2018). The rare omphacite relicts dispersed in this mesh have a distinct Omp3 composition ($\text{Di}_{68}\text{Jd}_{15}\text{Aeg}_{17}$; Figure 6b). No major-element analysis could be made on lawsonite, which is now completely pseudomorphosed by micas, plagioclase and subordinate chlorite and clinozoisite (e.g., Figures 4e and SM3f and SM3g). Clinopyroxene in late-stage veins, postdating both mylonitization and brecciation events, crystallized in equilibrium with talc and is $\text{Di}_{57}\text{Jd}_{22}\text{Aeg}_{21}$. Its major element composition is close to Omp3 (Figure 6b). In the metasomatic rinds, newly-formed garnet has a distinct core–mantle–rim zonation from $\text{Grs}_{17}\text{Prp}_{22}\text{Alm}_{61}$ to $\text{Grs}_{19}\text{Prp}_{26}\text{Alm}_{55}$ to $\text{Grs}_{18}\text{Prp}_{29}\text{Alm}_{53}$ (Figure 6h).

6.3. Intermediate Shear Zone

In the ISZ, the clasts of brecciated Fe-Ti metagabbro display the same mylonitic Omp1a-Omp1b zonation as observed in the LSZ. In contrast to the LSZ, no analogue of the omphacite-bearing M1 matrix could be found, whereas three generations of veins crystallized prior to the M2 brecciation event (Figures 6a). The first set of veins (Vein V0), folded inside the mylonitic foliation (e.g., Figure 4b), contains omphacite with composition $\text{Di}_{40}\text{Jd}_{38}\text{Aeg}_{22}$, directly comparable to that of Omp1b in LSZ Fe-Ti metagabbros and Veins V0. In Veins V1 (paragenesis: omphacite \pm apatite, always crosscutting the mylonitic foliation: Figures 4a, 4b, 4d, and 6e), omphacite cores also have Omp1b composition (Figures 6a and 6b), while the composition of Veins V1 rims is slightly enriched in the jadeite component ($\text{Di}_{40}\text{Jd}_{38}\text{Aeg}_{22}$; Figure 6a).

Omphacite from Vein V2 (observed only in the ISZ Fe-Ti metagabbros) and matrix M2 are very similar, with a composition of $\text{Di}_{50}\text{Jd}_{40}\text{Aeg}_{10}$ (comparable to Omp2b from LSZ). Omphacite is associated with garnet whose composition can be compared to Grt2a (cores, $\text{Grs}_{15}\text{Prp}_{22}\text{Alm}_{63}$) and Grt2b (rims, $\text{Grs}_{13}\text{Prp}_{27}\text{Alm}_{60}$) (Figures 6a and 6b), although M2 garnet is slightly depleted in grossular and almandine (Figures 6a and 6b) components. Locally, Cr contents of M2 omphacite and garnet are enriched up to wt. % concentrations with respect to those in M1, clasts, and veins of the LSZ (1.02 wt.% vs. 0.35 wt.%, respectively; refer to the complete database on SM5) and are directly comparable to the Cr concentration of M2-matrix crystals from LSZ. They also present the same peculiar enrichments, both fracture-like (observed in samples I35–15 and I38–15) and oscillatory (Figure 6g).

7. Trace Element Mineral Chemistry

To assess the trace element chemistry in detail, we measured some 210 spots in omphacite (approximately 70% from LSZ samples, 30% from the ISZ), 80 in garnet, 15 in ex-lawsonite, and 15 in apatite. To get rid of local bulk-rock compositional effect for data illustration in trace element distribution diagrams, the trace element compositions of the successive generations of minerals in clasts, high-pressure veins, and matrices were normalized to those of neighboring host eclogite/mylonitic clasts (e.g., mineral cores 1a) adjacent to eclogite-breccia layers. The complete data set is presented in SM5.

7.1. Omphacite

To lower the detection limits, the measurements on omphacite crystals were conducted using mainly 120 to 90 μm laser beam (and more rarely 44 and 60 μm); these beam diameters are larger than the dimensions of zoning in most crystals of matrices (e.g., Figures 3a–3e) and mylonitic clasts. Indeed, most of the LA-ICP-MS analyses include multiple zonations, and therefore, direct comparison between trace element geochemistry and single major components (e.g., for omphacite: jadeite, diopside, and aegirine) of matrix and vein omphacite is not feasible. Therefore, in samples L14–50, L14–53, L63–15b, and L63–15d, it was possible to identify the different signatures of cores and rims for mylonitic clast omphacites as well as for some omphacite crystals of the M1 matrix. For data illustration in trace element distribution diagrams, all omphacite compositions were normalized to Omp1a omphacite cores representing omphacite crystallization during prograde metamorphism and measured in the nearest clast or surrounding bulk rock.

Mylonitic clast. For Fe-Ti metagabbros in LSZ samples, omphacite rims (e.g., Omp1b generation) generally have similar concentrations in Sr, Pb, and V, with lower contents in Nb and As but higher contents of Ni (Table 2 and Figures 7a–7d). Contents of Cr and most FME are generally comparable for Omp1b and Omp1a (5–67 $\mu\text{g/g}$ of Cr; Table 2 and Figures 6b–6d), except for samples L14–53 and LS4–50 where Omp1b is richer in Cr and FME (Figures 6a–6d). LREE and HREE contents tend to be slightly higher and lower, respectively, in Omp1b compared to Omp1a. The Omp1b from clasts (*rims*) of samples L6315b and L6315d (Fe-Ti boudin W of Punta Forcion; Figure 7b) is slightly richer in REE, Y, Ni, Sr, and poorer in Co compared to those from other samples (Table 2 and Figures 7a–7d). In Mg-Al metagabbro clasts, Omp1b is enriched in Ba, Pb, Y, Ni, and HREE compared to Omp1a (Figure 7c). Interestingly, the samples from the ISZ are characterized by higher concentrations in REE, Cr, Ni, Pb, and Sr (Table 2) and lower LILEs, Nb, and As contents compared to the coeval Omp1a and Omp1b from the LSZ (Table 2 and Figure 7e). Trace element patterns are different from those in the LSZ: Omp1b tends to be depleted in Sr, Zr, Ni, and all REE and enriched in As compared to Omp1a.

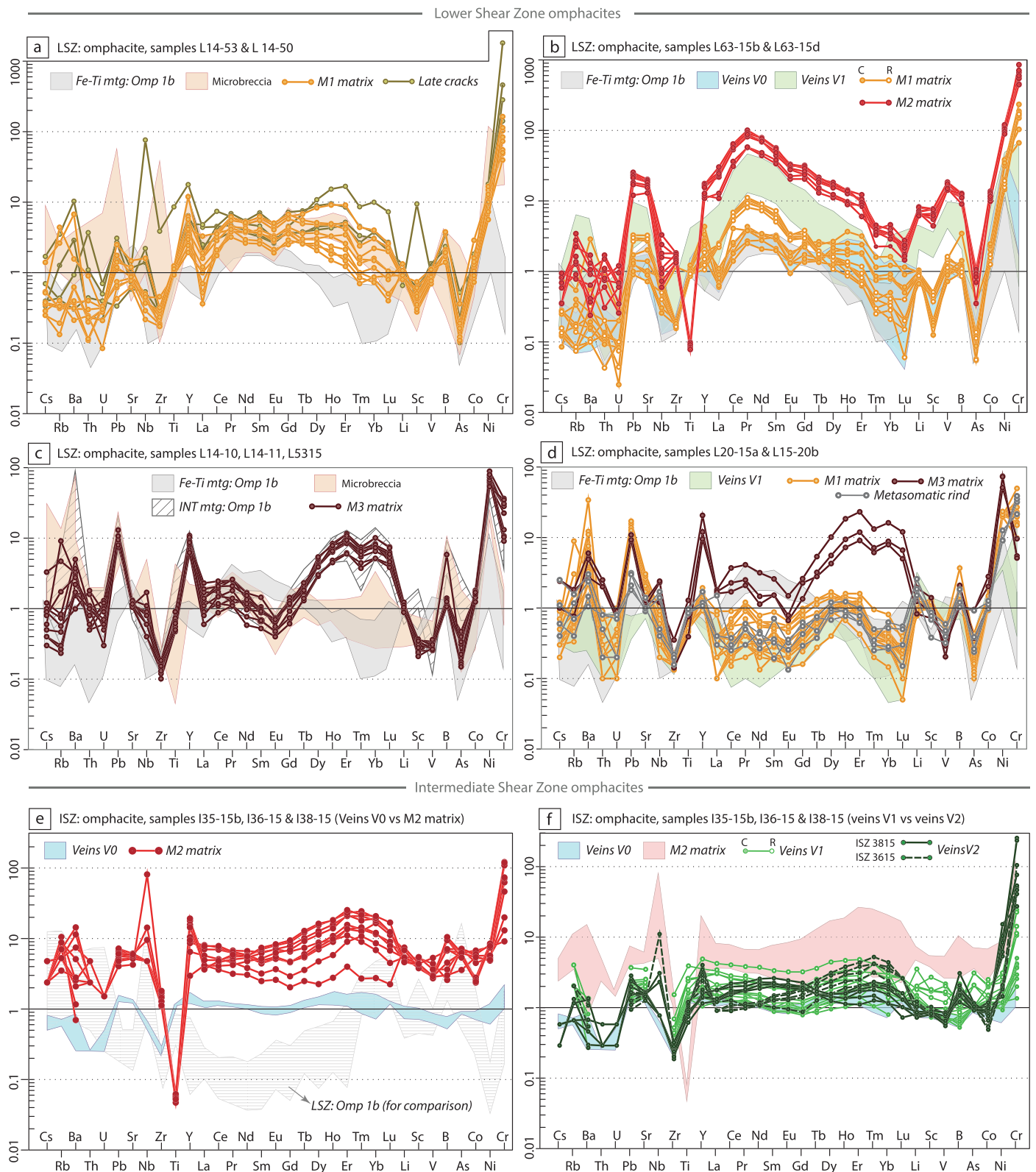


Figure 7. Trace element compositions of omphacite crystals from clasts, veins, and matrices (LA-ICP-MS analysis). Lower shear zone (LSZ): (a) samples L14–53 and L14–50 (east of Peiro Jauno peak); (b) sample L63–15b-d (base of Truc Bianco peak); (c) samples L14–10 and L14–11 (east of Rocce Sbiasere ridge), L53–15 (Prà Fiorito Valley); (d) samples L20–15a-b (Prà Fiorito valley). Intermediate shear zone (ISZ): (e, f) samples I35–15, I36–15, and I38–15 (Lago Superiore). For each diagram, data are normalized to the average of mylonitic omphacite Omp1a from adjacent, unbrecciated metagabbros. C = core; R = rim.

Veins V0. In the omphacite from veins V0 (generation: Omp1b) the concentrations of all trace elements are directly comparable to those of the rims of mylonitic clast grains with the exception of a slight increase in Y and Ni (LSZ samples; Table 2 and Figure 7b) and minor depletion in Zr and LILEs in ISZ samples (Table 2 and Figure 7e).

Matrix M1 and Microbreccia. Omphacite grains (generations: Omp2a and Omp2b) of M1 matrix show very similar compositions (Table 2 and Figures 7a, 7b, and 7d). Their trace element contents are very close to those of mylonitic omphacite rims (Omp1b), except for a marked enrichment in Cr and slight enrichments in Co, Ni, Pb, Sr, Y, and/or B depending on the sample (Figures 7a, 7b, and 7d). Conversely, As, La, and LILEs are depleted (Figures 7a, 7b, and 7d), except for the samples L20–15a and L20–15b (Figure 6d) which show marked enrichment in Rb and Ba (Table 2 and Figure 7d). In detail, the core-to-rim evolution of M1 matrix grains (e.g., Omp 2a: cores and Omp 2b: rims) is marked by an increase in Pb, Sr, Sc, and LREE concentrations with depletion in Y, Ni, and HREE (Table 2 and Figure 6b). The analyzed crystals from *microbreccia* domains (here Omp2b crystallizing around comminuted grains from clasts and the interstitial Omp2a; Figure 6e) show slightly higher LILEs concentrations, with marked positive anomalies in Pb, Zr, and Ni (Table 2 and Figures 7a and 7c). Increases in Li and Al₂O₃ contents are correlated in both *microbreccia* and M1-matrix omphacite (as well as in mylonitic clasts; SM4), showing that Li substitutes into pyroxene as spodumene (LiAlSi₂O₆) component. Broad positive correlations with CaO + MgO (SM4) indicate that Sr, light to middle REE (LREE-MREE), Co, and Ni partition with the diopside component of the pyroxenes.

Veins V1 (paragenesis: omphacite ± apatite), which crosscut the mylonitic foliation of clasts and are texturally postdated by M2 matrix (e.g., Figure 4a), show omphacite trace element patterns similar to those of Omp1b and/or M1 omphacite for most samples (L63–15b, L63–15d, L20–15, and L15–20; Figures 7b and 7d). For samples L63–15 (Figure 7b), the trace element pattern of V1 veins omphacite is parallel to that of M1 matrix omphacite but with enrichments in almost all elements. For ISZ samples, Veins V1 omphacite (e.g., Omp1b; Figures 6a and 6b) shows an enrichment in all elements from core to rim, in particular concerning Cr (Figure 7f).

Veins V2 (paragenesis: omphacite + garnet) are found only in the ISZ (e.g., Figures 4b and 4d). Veins V2 omphacites show compositions similar to those of Veins V1, but they are even richer in B, Ni, and Cr (Table 2 and Figure 7f).

Matrix M2. The trace element patterns of M2 matrix omphacite are quite parallel to those of M1 (and Veins V1 and V2) omphacite, but almost all elements are enriched by 0.5 to 1 order of magnitude (Figures 7b and 7e). In fact, there seems to be a progressive enrichment in almost all trace elements along the successive generations M1, Veins V1, V2, and M2 matrix (Table 2 and Figures 7b–7d and 7f). The sole exception is Ti, which in samples from both LSZ and ISZ is 1 order of magnitude lower than for all other omphacite crystallization stages (Table 2 and Figures 7b and 7e). The highest enrichments in M2 omphacite concern V, Ni, Co, and Cr (Table 2 and Figures 7b and 7e). For the latter, the measured concentrations by LA-ICP-MS reach wt.% levels (2,300–4,400 µg/g), which agrees with electron probe measurements. Boron and As are also enriched. M2 matrix omphacite from ISZ also displays a distinct positive anomaly in Nb, Y, and B, together with HREE/LREE enrichments (Table 2 and Figure 7e; for comparison with LSZ samples refer to Figure 7b). Lithium versus Al₂O₃ contents in both M2-matrix, Veins V1 and V2 omphacite do not correlate with the spodumene trend, contrary to those in clasts and M1 matrix (Figure SM4). Additionally, the lack of correlation of Sr and Sm with CaO + MgO (Figure SM4) suggests that the partitioning of these elements (and light to middle REE) did not follow the diopside component of the pyroxenes.

In *M3 matrix* (found only in the LSZ; samples L14–10 and L15–20; Table 2 and Figures 7c and 7d), the relict omphacite crystals show trace element patterns that are perfectly conform to each other despite the distance between the outcrop localities (Figure 1a). Figure 7c shows that M3 matrix omphacite has a composition close to that of Omp1b in intermediate metagabbro clasts and is even richer in Cr and Ni. Compared to mylonitic Fe-Ti metagabbro clasts, they are also enriched in Cr, Ni, Co (±B), Y, Pb, and HREE (with weak Tm negative anomaly) (Table 2 and Figures 7c and 7d). LILEs are generally enriched, with distinct Ba positive anomaly (Table 2 and Figures 7c and 7d), which is comparable to M1 omphacite. Lithium and Al₂O₃ contents broadly correlate, as well as CaO + MgO correlate with Sr (Figure SM4), though the respective patterns are different from those observed for mylonitic and M1 matrix omphacite.

Metasomatic Rind and Late-Stage Veins. Omphacite crystals from metasomatic rinds are directly comparable to those of M1 matrix, with a slight depletion in Pb and Ni (Table 2 and Figure 7d). Chromium, Ni, Co, and B are enriched compared to mylonitic clast Omp1a (Table 2 and Figure 7d) but remain considerably lower than M2 and M3 matrices, except Cr that is richer than in M3 (Figure 7d). For Late-stage Veins (Figure 7a), the omphacite is enriched in Cr, Ni, Sc, Nb, Zr, and REE compared to M1 Matrix. Lithium readily substitutes into pyroxene as a spodumene ($\text{LiAlSi}_2\text{O}_6$; Figure SM4) component; the positive correlations with $\text{CaO} + \text{MgO}$ (Figure SM4) indicate that Sr, Co, and, to a lesser extent, LREE-MREE, partition with the pyroxene component of the pyroxenes.

7.2. Garnet

In garnet, the analyses were run using 120-, 90-, and 60- μm laser beam, size that permitted in most cases to differentiate between rims and cores, except for the atoll-garnet crystals from samples L63–15b, I35–15, and I38–15 where the zonation thickness is too thin to analyze each rim. In trace element distribution diagrams, trace element compositions were normalized to clast garnets (Grt1a). In Fe-Ti metagabbro clasts, Grt1b is enriched in Y and HREE (Table 3 and Figures 8a and 8b), elements classically hosted in garnet (e.g., Spandler et al., 2003). Metallic elements such as Mn, Ti, and V are also enriched while Co, Ni, and Cr are very low in concentration (Table 3 and Figures 8a and 8b). Most LILE are also depleted in clast garnet from both the LSZ and ISZ (Figures 8a and 8b). Compared to Fe-Ti metagabbro garnet, that of Intermediate samples is slightly depleted in most LILEs (except for Rb) and LREE to MREE while enriched in Sr, Y, HREE, and Cr (Table 3 and Figure 8c).

While absent in M1-matrix, Veins V0 and V1, garnet from Veins V2 (ISZ only) shows patterns close to Fe-Ti metagabbro clast garnet (Figures 8a and 8b) but is depleted in LILE and REE for some samples and clearly enriched in Cr ($\pm\text{V}$ and B; Figure 8b).

Garnet from M2 Matrix shows trace element patterns parallel to those of Veins V2, with marked enrichments in all the FMEs, such as B, As, Li, Sc, V, Co, and Ni (Table 3 and Figure 8a and 8b). Chromium shows the highest enrichment (2 to 3 orders of magnitude respect to Fe-Ti metagabbros Grt1a) and reaches concentrations up to weight percent levels with cores generally richer than rims (Table 3 and Figures 8a and 8b). Rubidium, Zr, Nb, and Y are also enriched (the latter two more pronounced in the crystals from the LSZ) while Ti shows a clear drop (Table 3 and Figures 8a and 8b). Notably, the strong Cr enrichment and Ti drop (compared to Fe-Ti metagabbro clast garnet) is comparable to what is observed for M2 matrix omphacite from both shear zones (e.g., Table 2 and Figures 7b and 7e). The LREE/HREE ratios are broadly comparable to those of Veins V2 (Figures 8a and 8b), with core-to-rim HREE enrichments in the LSZ and uniformly high LREE/HREE ratios in the ISZ (but with constant depletion by 1 order of magnitude; Table 3 and Figures 8a and 8b). For all the generations, garnet MgO contents directly correlate with Co, Y, and REE concentrations while CaO broadly correlates with V (Table 3 and Figure SM4).

7.3. Apatite

Laser ablation on apatite crystals, usually run at the end of every measurement session with 90- and 60- μm beam sizes, was conducted with lower laser fluence at the sample site (10 J/cm^2) and slower repetition rate (8 Hz) to minimize the disruption of the crystals. Analysis from mylonitic clast shows the expected element partitioning, with enrichments in HFSE such as Th (up to $0.4 \mu\text{g/g}$), U (up to $0.3 \mu\text{g/g}$), Pb (up to $8 \mu\text{g/g}$), Y (up to $420 \mu\text{g/g}$), and Eu ($93 \mu\text{g/g}$), in agreement with literature data (e.g., Spandler et al., 2003), as well as high LREE/HREE ratios (Table 4 and Figure 9a). Both LILEs and FMEs are depleted, with the exception of As, which ranges between 3 and $4 \mu\text{g/g}$.

Apatite hosted in Veins V1 and M1 matrix have similar trace element trends (Table 4 and Figure 9a), although Veins V1 apatite is enriched in Rb, Sr, Ti, and HREE. Compared to the host rock and clast apatite, they are enriched in Th, U, Nb, As, Co, and Ni (Table 4 and Figure 8a), while Zr and Li are generally depleted. Both LREE and HREE show positive anomalies, while MREE are generally slightly depleted for M1 apatites (Table 4 and Figure 9a).

In M2 matrix, apatite shows trace element trends parallel to those of M1 matrix and Veins V1 (Table 4 and Figure 9a) but all trace elements are enriched by about 1 order of magnitude, except for Ba, Rb, Y, and MREE. Vanadium, B, As, and Cr (up to $23 \mu\text{g/g}$) show the highest enrichments (Table 4 and Figure 9a).

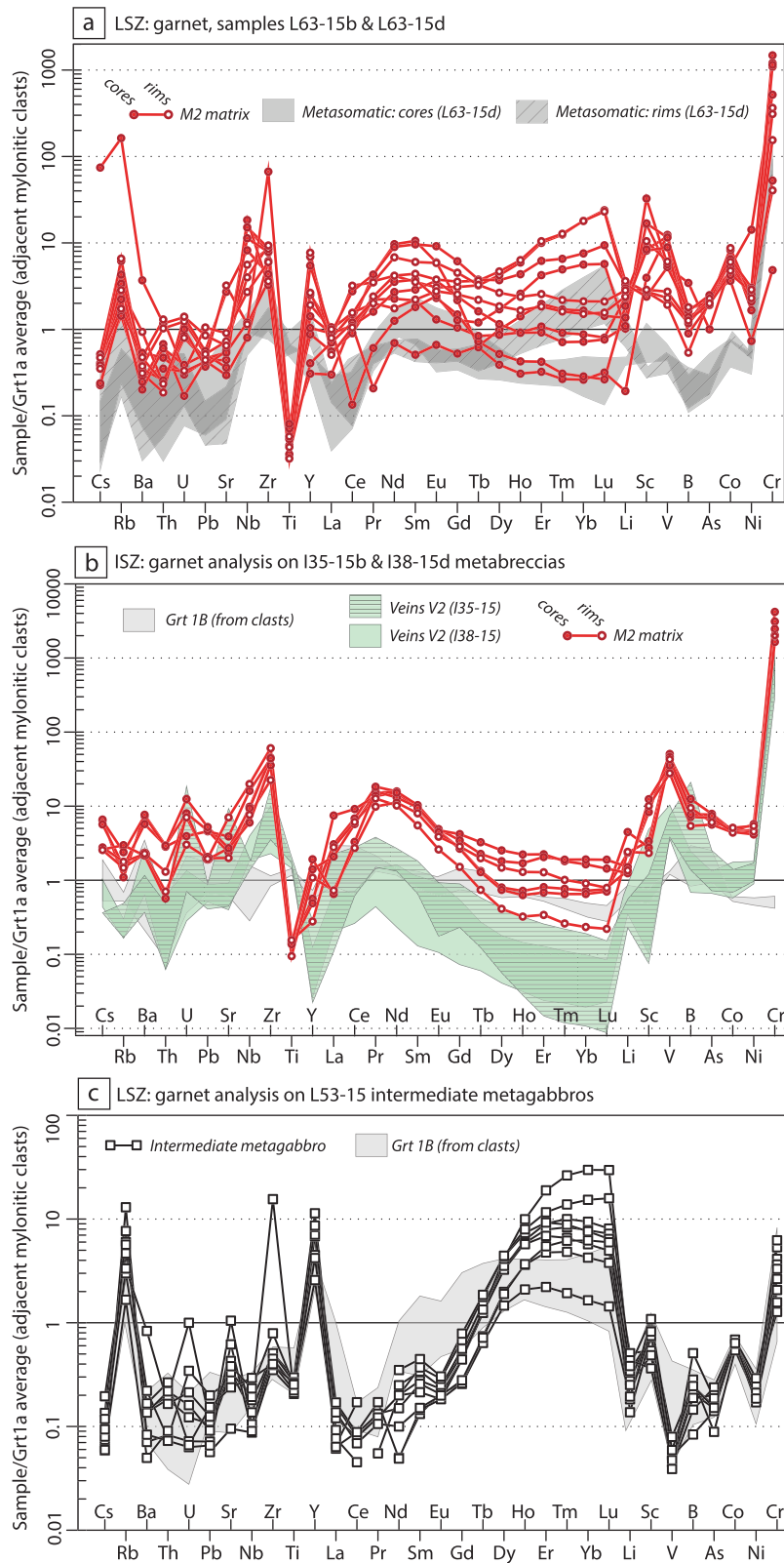


Figure 8. Trace element compositions of garnet crystals from clasts, veins, and matrices (LA-ICP-MS analysis). (a) Lower shear zone (LSZ), samples L63–15b and L63–15b (base of Truc Bianco peak). (b) Intermediate shear zone (ISZ), samples I35–15 and I38–15 (Lago Superiore). (c) Garnet crystals from intermediate metagabbros of sample L53–15 (Prà Fiorito valley). For each diagram data are normalized to the average of mylonitic garnet Grt1a from adjacent, unbrecciated metagabbros. C = core; R = rim.

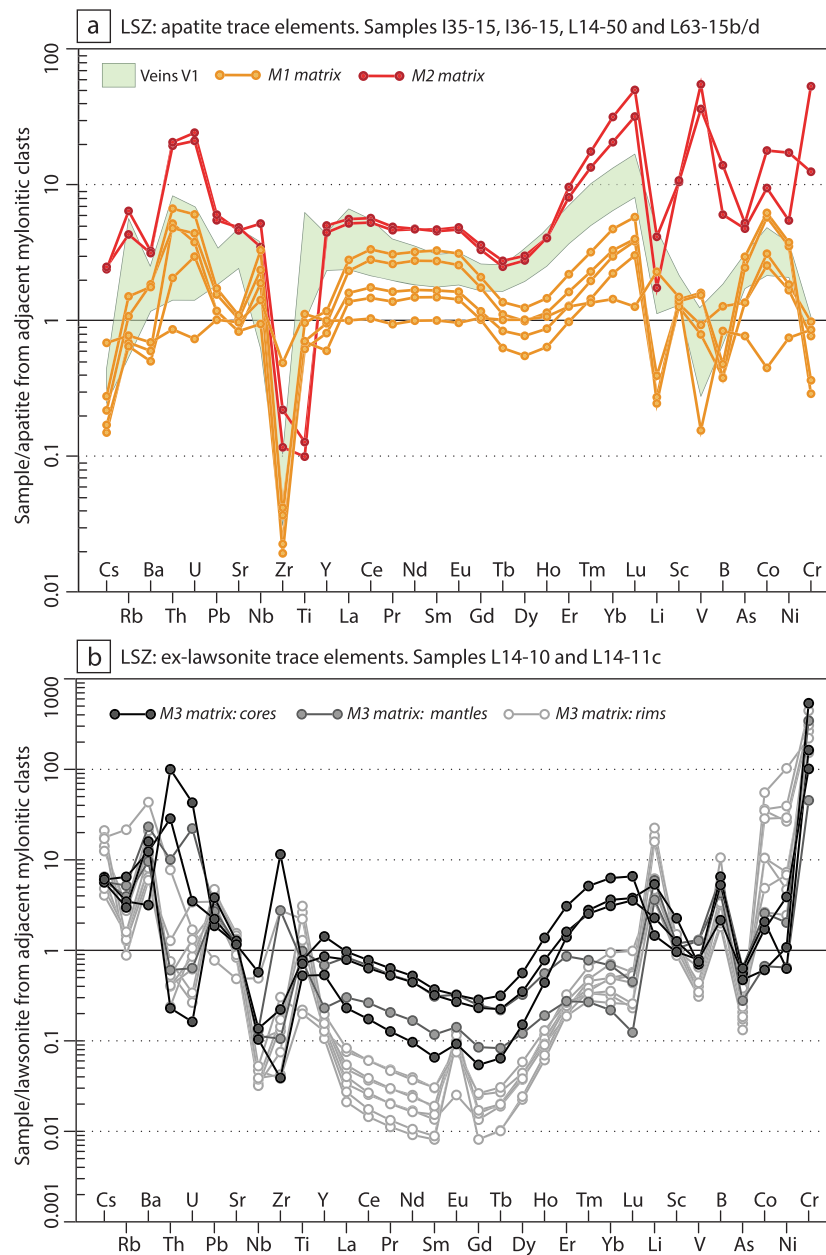


Figure 9. Trace element compositions (LA-ICP-MS analysis) of apatite crystals and lawsonite pseudomorphs. (a) Apatite crystals from veins V1 and matrices M1 and M2. The data are normalized to the average of apatite grains from adjacent, unbrecciated metagabbros. (b) Lawsonite pseudomorphs in M3 matrix (lower shear zone, east of Rocce Sbiasere ridge, samples L14-10 and L14-11). The data are normalized to the average of mylonitic ex-Lws from adjacent, unbrecciated metagabbros (e.g., Figure 4e).

As observed for both omphacite and garnet from M2 matrix, Ti has a strong negative anomaly (Table 4 and Figure 9a), here coupled to Zr depletion.

7.4. Lawsonite Pseudomorphs

Thanks to the exceptional size of the crystals (often >0.5 cm), the analyses on the pseudomorphosed lawsonite were run using 160- μm beam size, in order to obtain a bulk of their trace element signature. The pervasive replacement by epidote, plagioclase, and mica prevents any rigorous evaluation of the trace element concentration of former lawsonite but still allows an evaluation of the variation of the elements thought to be poorly mobile, such as Cr, Ni, and Co. For trace element distribution diagrams (Figure 9b), trace

element compositions of M3 matrix lawsonite were normalized to clast lawsonite from mylonitic Fe-Ti metagabbro clasts (sample L14–11c).

In M3 matrix, the lawsonite pseudomorphs have distinct zonations that correspond to three different geochemical signatures. Compared to clast lawsonite, M3 matrix lawsonite patterns show enrichments in Li, B, Pb, Co, Ni, and Cr (sample L14–11c; Table 5 and Figure 9b) and depletion in most REE, in particular LREE. This depletion is progressive from core to rim (1 order of magnitude lower; Table 5 and Figure 9b), and only rims show a positive Eu anomaly, possibly linked to recrystallization of plagioclase after lawsonite. Chromium and Ni contents have a distinct core-to-rim enrichment trend, with concentrations in the rims up to 2 orders of magnitude higher than the crystals from the clasts (Table 5 and Figure 9b).

8. Phase Equilibrium Modelling of Intermediate Metagabbros

Constraints on the P–T evolution and dehydration sequence of Monviso metagabbros involved in eclogite-facies brecciation are available in the literature only for Fe-Ti metagabbros and matrices (Angiboust, Langdon, et al., 2012; Groppo & Castelli, 2010; Locatelli et al., 2018). As brecciation occurred at the Fe-Ti/Intermediate metagabbro boundary, constraints on the dehydration sequence of Intermediate metagabbros are required. Consequently, a pseudosection for metagabbros with intermediate composition is herein modeled in the system NCFMASHTO. The bulk of sample L14-74a is a mylonitic, *intermediate-composition* metagabbro found at the transition between the intact block and the eclogitic breccia layer (e.g., Figures 3a and 3b). TiO_2 was considered due to the relevant presence of rutile in the mylonite (e.g., SM3g). The fluid phase was assumed to be pure H_2O , set in excess as suggested by (i) the occurrence of pseudomorphs after lawsonite (up to 11.5 wt% H_2O ; e.g., Pawley, 1994) in clasts (e.g., SM3g) and (ii) the occurrence in metagabbro clasts of healed garnet fractures (e.g., Angiboust, Langdon, et al., 2012; Broadwell et al., 2019; Locatelli et al., 2018), which at HP-LT is suggested to be promoted by fluid phase (Angiboust, Langdon, et al., 2012; Spandler et al., 2011). CO_2 was neglected, as no calcite crystallizes in the equilibrium eclogite-facies paragenesis. Considering the scarce amount of Fe^{3+} minerals in the eclogitic assemblage of sample L14-74a (ilmenite present only as exsolution in rutiles and < 30 vol% of omphacite with Aeg_{1-3}) a molar ratio of $\text{Fe}_2\text{O}_3/(\text{Fe}_2\text{O}_3 + \text{FeO})$ of 0.05 was imposed (inset in Figure 10a). The P–T pseudosections were calculated with *Perple_X* (software version 7.7.5; Connolly, 2005, Connolly, 1990) with the internally consistent thermodynamic data set *hp04ver.dat* (Holland & Powell, 2003, 1998). Mineral solid-solution models were Omph (GHP) for omphacite (Green et al., 2007), Ep (HP) for epidote/clinozoisite (Holland & Powell, 1998), Gt (HP) for garnet (Holland & Powell, 1998), cAmph (DP) for amphibole (Diener et al., 2007), Chl (HP) for chlorite (Holland & Powell, 1998), Mica (CHA) for phengite (Auzanneau et al., 2009; Coggon & Holland, 2002) feldspar for ternary feldspar (Fuhram & Linsley, 1988) and the ideal solution “T” for talc. H_2O fluid solution model is from Holland and Powell (1991, 1998). The obtained pseudosection is dominated by trivariant and quadrivariant fields, with a few divariant and quinvaryant fields, and is shown in Figure 10a. The P–T conditions were constrained by comparing predicted garnet isopleths with selected mineral compositions (Tables 2 and 3). All the P–T estimates on Figure 10a incorporate typical uncertainties on EMPA measurements, ~3% to ~5% (Lifshin & Gauvin, 2001). The constrained P–T stability field for intermediate metagabbros is marked by thermodynamic equilibrium between ~2.4 and 3.0 GPa at temperatures of ~470–520 °C (Figure 10a). The pretty large modeled equilibrium field is characterized by the sudden disappearance of glaucophane and progressive decrease of lawsonite combined with increases in the modal volume of garnet and omphacite (Figures 10b and 10c). The onset of garnet crystallization coincides with a quick drop of rock molar volume (Figures 10b and 10c) and marks the onset of rapid decrease in the global H_2O content of the rock, predicting fast dehydration and related fluid liberation. Remarkable agreement exists between the modeled modal volume of minerals and the one observed in the rocks (Figure SM3g). P–T estimates for *intermediate* metagabbros are also comparable (Figure 10c) to those retrieved for eclogitic Fe-Ti metagabbro mylonitization and brecciation (Locatelli et al., 2018).

9. Discussion

9.1. Fingerprinting Brecciation Events and Fluid Sources

Trace element redistribution between host-rock, vein, and matrix minerals is controlled by mineral/fluid partition coefficients, mineral major element compositions and the composition of the coexisting fluid

Intermediate metagabbro (L14-74A) H₂O saturated

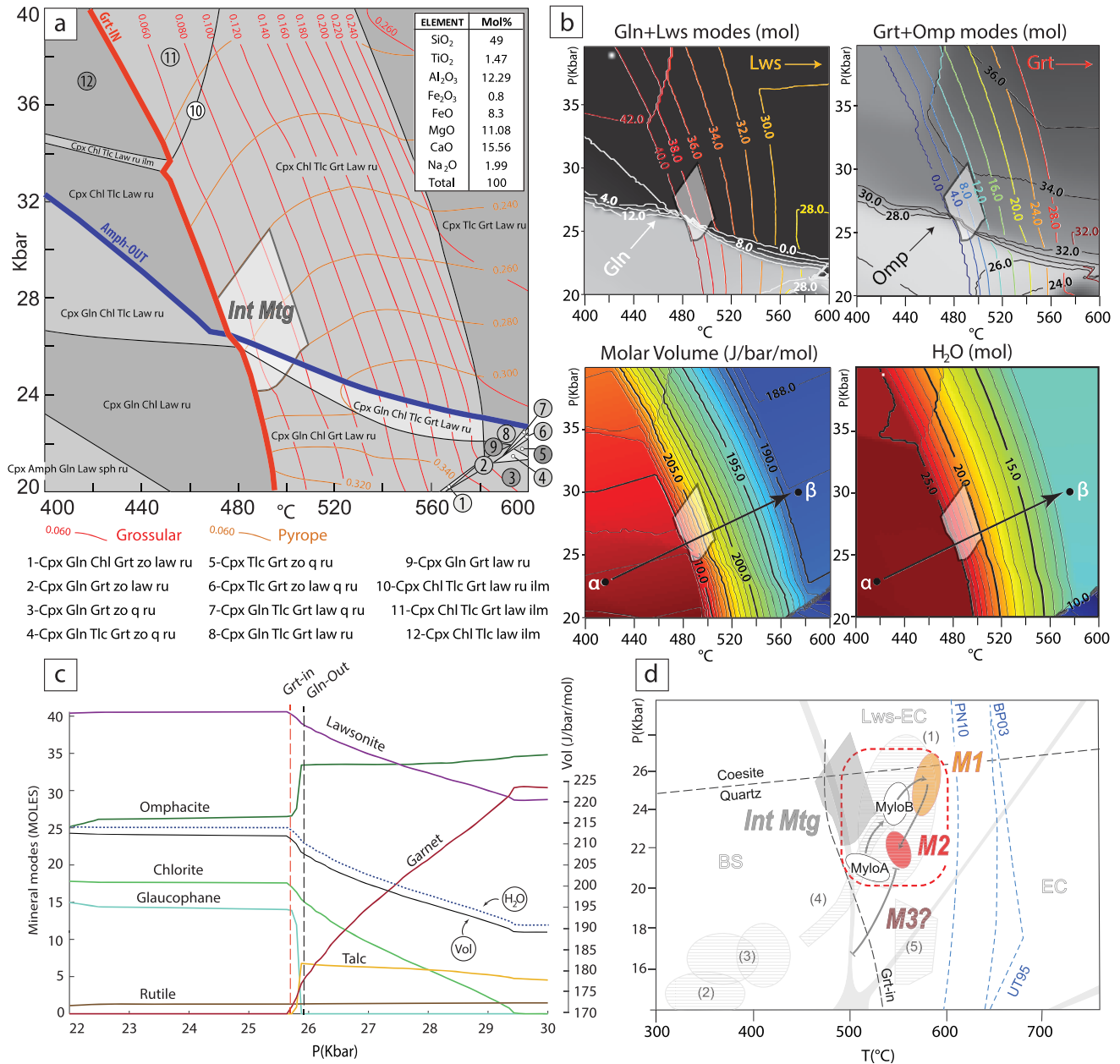


Figure 10. P–T estimates for the studied intermediate metagabbro (sample L14-74a), inferred from PerpleX pseudosection modeling in the system NCFMASHTO. P–T condition boxes consider approximately 5% calculated uncertainties. Composition used for modeling is in the table inset of Figure 10a (upper right corner) and the complete rock analysis is in table 1. Abbreviations: Amph: Amphibole; Lws: Lawsonite; Omp, omphacite; Gt, garnet; Chl: Chlorite; zo: Zoisite; ru: Rutile; Tlc: Talc; ilm: Ilmenite; grs, grossular; PrP: Pyrope; Cpx: Clinopyroxene; q: Quartz; sph: Shene; M1, matrix M1; M2, matrix M2; M3: Matrix M3; a and B mylonitic steps; Int Mtg: Intermediate metagabbros. (a) P–T estimates for the prograde mylonitization of intermediate metagabbros. (b) Maps showing variations of mineral modes (Mol), molar volume (J/bar/Mol), and water amount (Mol) modeled for sample L14-74a. (c) Variations of mineral modes (Mol), molar volume (J/bar/Mol), and water amount (Mol) along the profile α - β , showing the rapid change in molar volume and water content of the system at the onset of garnet crystallization and glaucophane destabilization. (d) Estimated P–T trajectory from pseudosection modeling, integrated with the estimations of mylonitic steps 1 and 2 (Fe-Ti metagabbros) and matrices M1–M3 (all samples from the LSU: Locatelli et al., 2018). The red, dotted-line box represents the P–T estimates considering uncertainties on bulk composition; the thin, gray arrows suggest the relative chronology of mineral parageneses obtained from textural evidences. Additional data sets from works on the Monviso and Schistes Lustrés areas: (1) Lago Superiore unit, Monviso: Angiboust, Agard, et al. (2012) for peak and retrograde conditions; (2) and (3) west and east Schistes lustrés: Agard et al. (2009); (4) prograde eclogitization P–T path of Monviso metagabbros: Groppo and Castelli (2010, 2010); (5) Monviso metagabbros and metabasites: Schwartz et al. (2000). Blue, dotted lines represent the experimental dehydration curves for antigorite; BP03, Bromiley and Pawley (2003); UT95, Ulmer and Trommsdorff (1995); PN10, Padrón-Navarta et al. (2010). Metamorphic facies: Lws-EC: Lawsonite-bearing eclogite facies; BS: Blueschist facies; EC: Eclogite facies.

phase(s). In the following, geochemical patterns for each vein and matrix are combined to constrain the fluid composition and provenance associated with the successive veining and brecciation steps (compare Figure 1 d). A genetic summary is presented in Figures 11a–11f.

9.1.1. Crystallization of Veins V0: Evidence for Equilibrium With Local Fluid (Step a)

Veins V0 predate brecciation (Step A; Figure 11a). Their omphacites show major element compositions similar to those crystallizing as rims in the adjacent host-rock and mylonitic clasts (Omp1b; Table 1 and Figures 6a and 6b), suggesting that they formed during the prograde path, close to eclogite-facies PT conditions (MyloB in Figure 10d; Locatelli et al., 2018). Their trace element patterns also resemble Omp1b, with only slight variations between vein/host-rock pairs from different outcrops (Figures 7b, 7e, and 7f). Omphacite cores from Veins V1 in the ISZ (e.g., Figure 4a) have trace element patterns comparable to V0 (Table 2 and Figure 7f) and could therefore be ascribed to the same event. These similarities support chemical equilibrium between omphacite in the veins and in the host rocks, at least at the centimeter scale. This suggests that the formation of V0 was assisted by fluids locally released from neighboring Fe-Ti metagabbros toward the end of the prograde path, that is, mainly the glaucophane-out reaction (to form Omp1b; MyloB in Figure 10b). Our observations agree with the independent results of Nadeau et al. (1993), Philippot and Selverstone (1991), Philippot and van Roermund (1992), and Spandler et al. (2011), who found no evidence of external fluid involvement during vein formation in the ISZ.

9.1.2. Crystallization of Matrix M1 and Veins V1: Evidence for Decimeter-Scale Fluid Circulation (Step B)

The first brecciation event (Step B; Figure 11b) is recorded by both microbreccia and omphacite-rich M1 matrix in the LSZ, while only witnessed by the crystallization of omphacite + apatite Veins V1 in the ISZ. The slight differences in trace element contents between omphacite from clast mylonite (Omp1b) and M1 matrix Omp2a/2b (the latter being enriched in Cr, Ni, Co, Pb, and Sr; Figures 7a, 7b, and 7d) suggest that M1 mineral composition, unlike Veins V0, was not completely buffered by locally derived fluid in equilibrium with Fe-Ti metagabbros. Rather, infiltration of (probably small amounts of) an external fluid could account for the observed geochemical trends. Infiltration of some external fluid is also supported by the wide compositional range of M1 matrix omphacite (Figure 5b), the complex overgrowth of Omp2b over Omp2a (e.g., Figure 5c) and the complex trace element core-to-rim zoning (Table 2 and Figures 6a, 6b, and 6d).

Considering that the M1 matrix composition approaches that of Intermediate metagabbros for both major (MgO, CaO, FeO; Figure 5a and Table 1) and trace elements (M1 enriched in Cr, Ni, Co, Li, Rb, Sr, Th, and U compared to Fe-Ti metagabbro clasts; Figure 5d), a fluid contribution originating from or equilibrated with Intermediate metagabbros is most likely. Another potential fluid source is serpentinites underlying the metagabbros but this can probably be discarded here because (i) the bulk M1 matrix Cr and Ni concentrations reach those of Intermediate gabbros but remain considerably lower than for serpentinites (e.g., Tables 1 and 2 and Figures 5d–5f, 7a, 7b, and 7d), and (ii) M1 matrix contents of B, As, Sb, and U (typically enriched in ocean floor derived serpentinites; Kodolányi et al., 2012; Peters et al., 2017) remain low compared to those of serpentinites (Figure 5d; see also Hattori & Guillot, 2007; Spandler et al., 2011; Angiboust et al., 2014).

Geochemical patterns thus suggest that the M1 matrix crystallized in the presence of a fluid emanating from the Intermediate metagabbros surrounding the Fe-Ti metagabbro breccia planes (which themselves represent former sills or dykes; Locatelli et al., 2018). This explanation is consistent with pseudosection modeling results showing that M1 formation can be ascribed to peak P–T conditions (Figure 10; Locatelli et al., 2018; omphacite composition Omp2a/2b; Figures 6a and 6b) and that Intermediate metagabbros still contain hydrated phases at peak conditions (Figures 10a and 10d), contrary to Fe-Ti metagabbros.

Pseudosection modeling suggests that both the glaucophane-out (mainly forming omphacite and talc) and garnet-in (from lawsonite and chlorite destabilization) reactions likely occurred in the Intermediate metagabbro at peak conditions (Figure 10c). In these reactions, garnet and lawsonite are the main trace element hosts: The (partial) destabilization of lawsonite releases Pb, Sr, and most REE to the fluid phase (Martin et al., 2014), while garnet growth results in HREE and Y sequestration (Figure 8c) and, therefore, high LREE/HREE ratios in the fluid at equilibrium, which is in good agreement with the geochemical signal of M1 matrix (Tables 1 and 2 and Figure 5c).

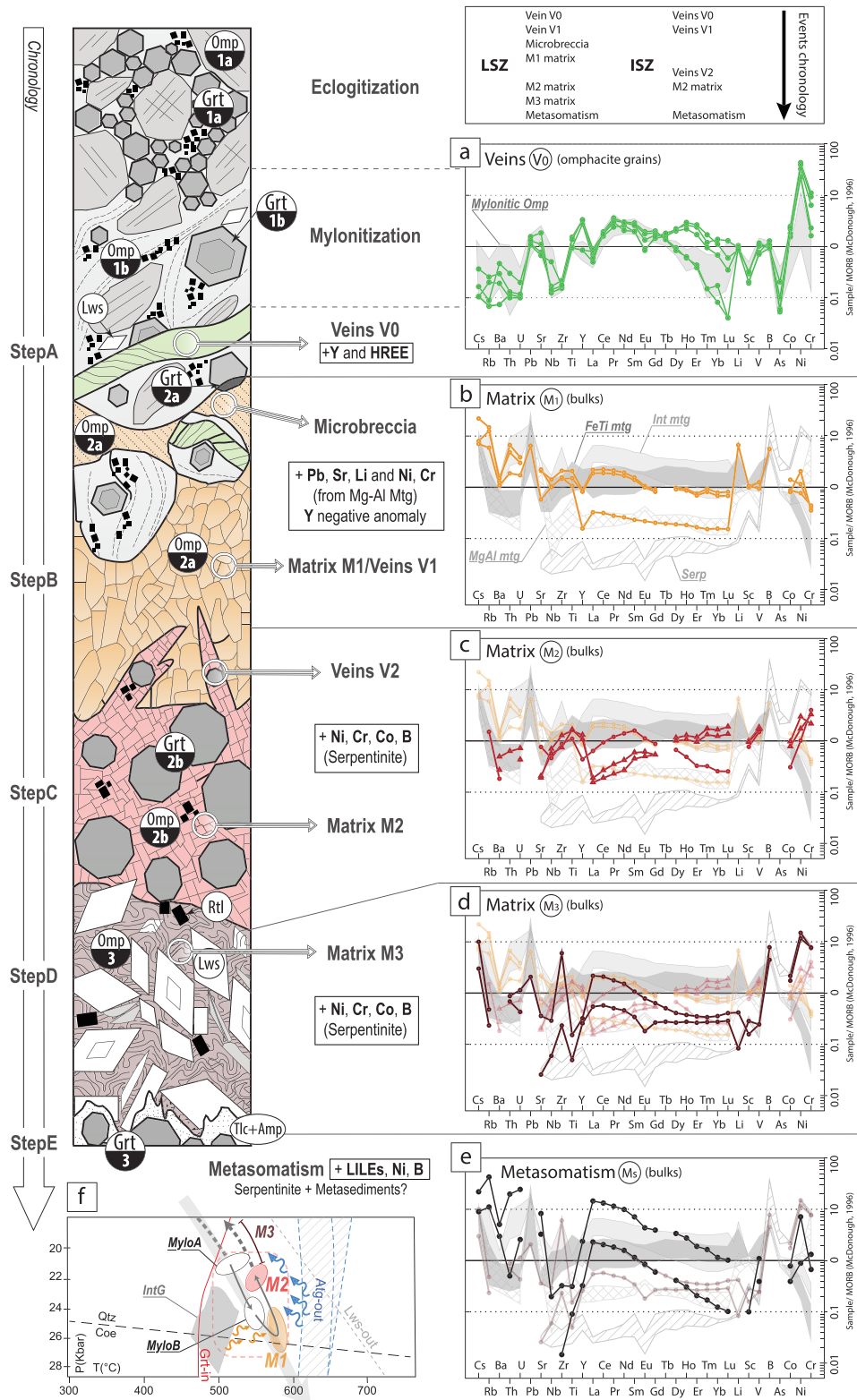


Figure 11. Sketch of the successive vein and matrix generation formation, combining textural domains observed in the eclogite-facies breccias from Monviso (left, not on scale), mineral generation from its composition (circle labels), and the associated trace elements patterns (diagrams a–e). (a) Trace element diagrams (LA-ICP-MS analysis) of omphacite crystals from veins V0. (b–e) Trace element diagrams for bulk compositions of matrices M1–M3 and metasomatic rinds, respectively. (f) Calculated P–T conditions for the successive paragenesis of the Lago Superior unit and schematic potential fluid sources (thermobarometric data from Locatelli et al., 2018).

9.1.3. Crystallization of M2 Matrix and Veins V2: Evidence for Mixed-Fluid Sources (Step C)

Formation of the M2 matrix (Step C; Figure 11c) composed of omphacite, garnet, and accessory talc and apatite (e.g., SM3c; refer also to Locatelli et al., 2018) postdates the crystallization of Veins V0 to V2, microbreccia, and M1 matrix (e.g., Figures 2c, 3f, and 11c). The similar omphacite (Omp2b) and garnet (Gt2) compositions in both the V2 Veins and M2 matrix nevertheless advocate for crystallization at comparable P–T conditions.

The geochemical signature of M2 matrix shows some similarities with that of M1: Its bulk composition is close for both major and trace elements (Figure 5d), and omphacite trace element patterns are broadly parallel although enriched by 1–1.5 orders of magnitude in almost all elements (except Ti; Figures 7b and 7e), particularly Pb, Sr, Li, Sc, and V. However, the major Cr enrichment of the M2 matrix (and Veins V2) contrasts with previous matrix and vein generations: It is higher than that of M1 and Intermediate metagabbros by at least one order of magnitude and trends toward that of serpentinites (Figures 5d and 5e). Similarly, both omphacite and garnet (and apatite to a lesser extent) are enriched in Cr by 2–3 orders of magnitude compared to clast minerals (Figures 7 and 8), reaching weight percent concentrations and showing peculiar oscillatory textures of Cr-enrichment (Figures 6g and 6h). The enrichment in Cr and to a lesser extent in Ni, Co, B ± As, and LREE to MREE patterns in bulk, omphacite, garnet, and apatite (Tables 1, 2, 3, 4, and SM5 and Figures 6, 7b, 7e, 8a, 8b, and 9a) is typical of serpentinite-derived fluids. Their contribution was detected by Hattori and Guillot (2007) and Spandler et al. (2011) for the Monviso and is commonly observed in similar geological settings (e.g., Deschamps et al., 2013; Hattori & Guillot, 2007; Scambelluri et al., 2004). The lack of correlation between trace and major components for M2 matrix and Veins V2 omphacite (e.g., spodumene and diopside; Figures SM4e–SM4g) is consistent with external fluid infiltration.

Two dehydration reactions are proposed for serpentinite: (i) the *antigorite-out* reaction, Antigorite → Forsterite + Enstatite + Chlorite + H₂O, occurring at 640–520 °C and ~2–5 GPa (Bromiley & Pawley, 2003; Ulmer & Trommsdorff, 1999) and (ii) the *brucite-out* reaction, Brc + Atg → Ol + H₂O, occurring at ~500 °C and 1.5–2.0 GPa (Scambelluri et al., 1991; Ulmer & Trommsdorff, 1999). Only the brucite-out reaction was crossed in the Monviso serpentinite sole, given the absence of chlorite harzburgites that is consistent with the peak P–T conditions for this unit (Locatelli et al., 2018). Rare olivine-bearing veins (expected as a consequence of brucite breakdown; e.g., Scambelluri et al., 1991) cutting across the serpentinite have indeed been identified in some massive serpentinite blocks scattered in the LSZ (Groppo & Compagnoni, 2007) and more recently in the basal serpentinites (Gilio, 2017). Local serpentinite dehydration can thus account for the serpentinite-derived fluid infiltrations accompanying M2 matrix formation. However, the scarcity of olivine veins suggests only minor fluid release, so that serpentinite-derived fluids may also come from the antigorite-out dehydration reaction in deeper portions of the subducting slab.

9.1.4. Crystallization of Matrix M3: Evidence for External Fluid Circulation (Step D)

The third, volumetrically dominant, lawsonite-rich M3 matrix (80 vol% of matrices; Step D; Figure 11d) is found only in eclogitic breccia blocks from the LSZ (refer to Figure 3a and Table SM1), in the core of breccia planes, and cuts across all preexisting structures of the brecciated blocks (e.g., Figures 2c and 3e). The M3 matrix has a major element composition remarkably close to that of serpentinites (i.e., FeO, MgO, and alkalis; Figure 5a). The trace element trends and concentrations for the bulk M3-matrix also considerably differ from those of neighboring Mg–Al and Fe–Ti metagabbros (Table 1 and Figure 5d), with strong enrichments in Cr, Ni, and Co reaching serpentinite concentrations (Table 1 and Figures 5c and 5d) and depletion in most HFSE and LILE, notably in P, Sr, Nb, Zr, and Rb (Table 1 and Figures 5c–5f). Compared to clast minerals, omphacite relics show marked enrichments in Ni (2 orders of magnitude), Cr, and HREE, and Cr in lawsonite pseudomorphs is enriched by 3 orders of magnitude (Tables 2 and 4 and Figures 7c, 7d, and 9b). For the latter, the core-to-rim zonation in the pseudomorphs domains after lawsonite shows a progressive enrichment (up to 3 orders of magnitude) in B, As, Co, and Ni (Table 4 and Figure 9b), suggesting progressive increase in external fluid influx during M3 matrix crystallization.

The ultramafic geochemical signature of the M3 matrix, exotic with respect to neighboring metagabbros, points to infiltration of a serpentinite-derived fluid. Pseudosection modeling indicates that the M3 matrix formed on the retrograde path of the Lago Superiore Unit (yet in the lawsonite stability field; Locatelli et al., 2018), making the contribution of local dehydration reactions unlikely. The M3 matrix (Step D; Figure 11e), therefore, attests to the infiltration of important amounts of external fluid (judging from the large amount of lawsonite pseudomorphs observed). We propose that these fluids derive from serpentinite

dehydration (antigorite-out reaction) in deeper portions of the subducting slab, that is, higher than 2.8 GPa and 600 °C given the Monviso P–T regime (Figure 10d).

9.1.5. Postbrecciation Evolution (Step E)

Further fluid ingress after the M3 brecciation event is evidenced in the LSZ (Step E; Figure 11e) by (i) extensive metasomatism on brecciated blocks, once detached and embedded in the LSZ, with prominent rind formation (at their contact with the antigorite-rich matrix embedding them; Angiboust et al., 2014) and (ii) opening of HP “Late-stage veins” (e.g., Figure SM2c). In the metasomatic rinds, the preexisting eclogite facies assemblage was gradually replaced by a mafic to ultramafic assemblage (chlorite + garnet + talc + sodic amphibole ± diopside + albite + epidote + rare phengite after lawsonite; Figures SM3f and SM3g). Mineral assemblage and trace element concentrations from both bulk rocks and omphacites (Table 2 and 3 and Figures 5d, 7c, and 7d) suggest an interaction with ultramafic fluids (e.g., enrichment in Co, Ni, Cr, and Mg in the rinds along with elevated U/Th; Figures 7c and 7d) and possibly metasediments-derived fluids too (the preferential carrier of LILEs and HFSE; Figures 7c and 7d). The latter has strong enrichments in metasomatic rinds, if compared to the host rocks from the LSU (Figures 4c and 4d) and the M1, M2, and M3 matrices, with Cs, Rb, Ba, Th, and U enriched up to 2 orders of magnitude (Table 2 and Figure 4d). The absence of Li enrichment in both M3 matrix and metasomatic omphacite (the major Li host-mineral in such lithologies; e.g., Spandler et al., 2003; Angiboust et al., 2014) suggests that the percolating “deep” subduction fluids were not specifically enriched in Li at this stage, in line with studies on other Alpine HP shear zones (e.g., Halama et al., 2014; Scambelluri et al., 2004) or from the Franciscan complex (Penniston-Dorland et al., 2010).

9.2. Progressive Shear Zone Formation: Pathways and Scale of Fluid Migration During Subduction

The geochemistry of the successive vein and matrix generations in the studied shear zones illustrates the progressive opening of the system, from a closed system in which rocks show equilibrium with a locally released fluid (Step A: V0 veins; Figure 11a) to increasing amounts of external fluid, first from the surrounding Intermediate metagabbros (Step B: M1 matrix, decimeter-scale fluid ingress; Figure 11b), then through larger-scale serpentinite-derived fluid infiltration (M2 and mainly M3, Steps C and D; Figures 11c and 11d). This is also reflected by the volumetric increase of matrices, increasing from M1 to M3, and suggests an evolution of the effective permeability through brittle deformation and strain localization (Figures 12a–12d).

In eclogitic breccia clasts and Fe-Ti metagabbros (LSZ and ISZ), Veins V0 form syntaxial crack-seal fractures (Step A; Figures 12a and SM2d), either folded (e.g., Figures 4b and 4e) or sheared in the S1 mylonitic foliation (e.g., Figure SM3b), in which omphacite is at chemical equilibrium with mylonitic omphacites (e.g., Omp1b; Table 2 and Figures 7b and 7f). This supports omphacite growth through repeated crack-sealing cycles and diffusional mass transfer through a rather stagnant fluid, locally released along prograde dehydration reactions (MyloB in Figure 10). This scenario is analogue to what Philippot and Selverstone (1991), Philippot and van Roermund, (1992), and Spandler et al. (2011) proposed for the omphacite-bearing veins in the ISZ (i.e., “Type1” of Spandler et al., 2011).

The first (strongly localized) brecciation event (i.e., M1 matrix, Step B; Figure 12b) resulted in intense metagabbro fragmentation (with decimeter- to millimeter-sized clasts; e.g., Figures 3d, 3e, and 4b–4d) and comminution of crystals from mylonitic clasts, which were then overgrown by newly crystallized omphacite with infiltration-like geometries (Omp2a and Omp2b compositions respectively, microbreccia; Figure 6e). These textures suggest that brecciation induced transient, anisotropic permeability increase in the Fe-Ti metagabbros to permit decimeter-scale fluid ingress (Figure 12b). Meter- to- hectometer-scale ingress of external, serpentinite-derived fluids occurred in both the LSZ and ISZ during M2, although in limited amounts, given the moderate changes in geochemical patterns (Figure 11c). This may have taken place through multiple fluid pulses, as revealed by the complex oscillatory zoning and fracture-like patterns of Cr enrichments in both V2 and M2 garnets (e.g., Figures 4b and 6g).

The presence in the M3 matrix of numerous clasts containing the M1 + M2 matrices (Figures 3e and 4e) and penetrative fracturing of the core of breccia planes (Figure 2c) indicate that M3 brecciation preferentially developed on former breccia horizons (Step D; Figure 12d). The impressive amount of hydrated minerals (i.e., lawsonite pseudomorphs and talc) in M3 compared to the rather dry M1 and M2 matrices, and its clear ultramafic geochemical signature (Figures 5 and 11d), advocate for a significant, likely progressive (i.e., core-

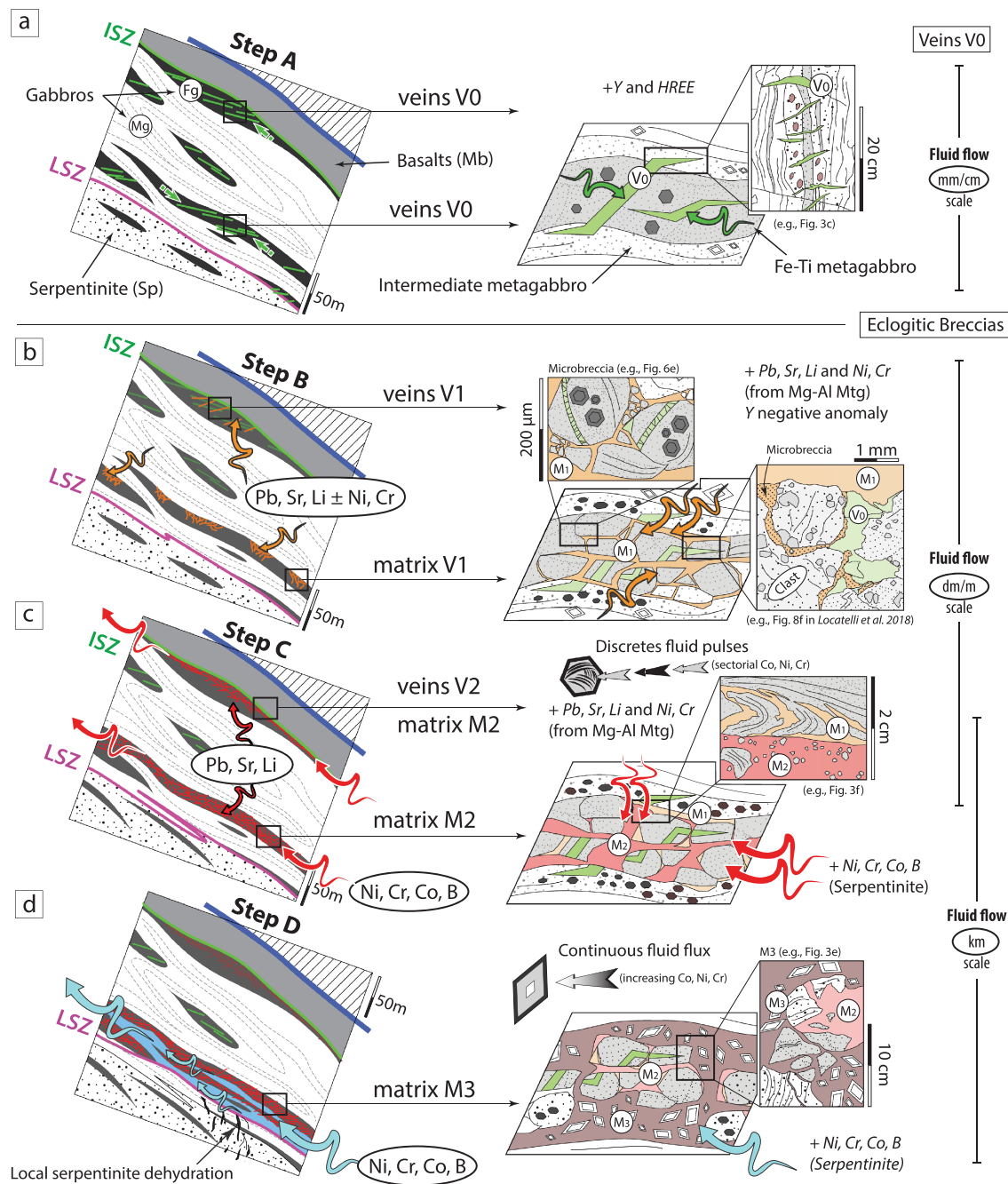


Figure 12. Chronological scheme of the successive veining and brecciation steps leading to the formation of Monviso eclogitic breccias. (a) Step a: Development of omphacite ± apatite-bearing veins V0 in Fe-Ti metagabbros. Their major- and trace-element composition at equilibrium with that of the host-rock (Fe-Ti metagabbro) suggests local equilibrium with a rather stagnant fluid (closed system, mm to cm scale mass transfer) produced locally by prograde dehydration reactions. Note the tapered geometry of these veins, which disappear at the contact with the intermediate metagabbro. Notable examples are in block B70, Prà Fiorito Valley. (b) Step B: First brecciation step accompanied by crystallization of M1-matrix. Omphacite crystallizes both as hypidiomorphic grains (e.g., Figure 5a) or as newly-formed, “infiltrating” omphacite generation crystallizing around comminuted mylonitic fragments (microbreccia domains; e.g., Figure 7e). Trace-element composition, with enrichment in Pb, Sr, li, Ni, and Cr, suggests that fluids promoting M1 crystallization were derived from surrounding intermediate metagabbros (garnet-in reaction), rather than Fe-Ti metagabbros or serpentinites. (c) Step C: Crystallization of M2 matrix cross-cutting M1 matrix, recognizable in the samples by its paragenesis of omphacite + garnet, the latter absent in M1-matrix. Trace element composition of M2 matrix suggests limited infiltration of serpentinite-derived fluids (evidenced by the strong, typically ultramafic enrichment in mg, Ni, Cr, B, and high LREE/MREE). It marks therefore the opening of the system to external fluid infiltration, with brecciation over the entire length of the LSZ and ISZ. (d) Step D: From blocks dispersed only in the LSZ, it is evident that the lawsonite-rich matrix M3 postdates all the preexisting breccia-structures, notably both the brecciation events M1 and M2. High B, co, Ni, and Cr concentrations, coupled with V, Sc, li, Pb, and Sr anomalies support the hypothesis of massive amounts of externally, serpentinite-derived fluids circulated at that stage. Thus, the crystallization of M3 matrix marks the large-scale fluid flux (derived only by external sources) and the partitioning of strain into the LSZ, leaving the ISZ “frozen.”

to-rim enrichments in lawsonite pseudomorphs; Table 4 and Figure 9b) increase in fluid circulation and for the formation of a high (and transient?) permeability zone in the eclogitic metagabbros that channelized large-scale circulation of external fluids.

The M3 matrix composition calls for fluids derived from extensive antigorite dehydration, hence from at least 10–20 km deeper (Figure 10d; see also Angiboust et al., 2014), confirming that M3 breccia planes were then fully connected over the whole LSZ (i.e., 15 km; Locatelli et al., 2018), contrary to M1 and M2. Consistently, M3 is absent from both the undetached breccia layers of Truc Bianco (at the base of the Mg-Al metagabbro cliff; Figure 1d) and the ISZ, where breccia levels are observed at the top of the Mg-Al metagabbros but show no dismembering after M2.

M3 brecciation and associated fluid circulation (Step D; Figure 10d) is therefore the key event that controlled further weakening and achievement of kilometer-scale connectivity in the LSZ, associated to the contemporaneous deactivation of brecciation in the ISZ. Further strain localization in the LSZ (Step E) resulted in the progressive shear zone broadening with dismemberment and incorporation of breccia blocks into the metasomatic serpentinite-rich matrix (e.g., Figures 1b–1g). The LSZ developed by network widening (e.g., Schrank et al., 2008) rather than by extensive mixing along the subduction interface (Blake et al., 1995; Festa et al., 2019; Guillot et al., 2004). This is attested by (i) eclogite-breccia layers in the largest Type 2 blocks and lenses systematically oriented toward the cliff of intact Mg-Al metagabbros, hence subparallel to the roof of the LSZ and with only limited rotation after their “decollement” (e.g., Punta Murel, Colle di Luca and Alpetto Lake; Figures 1b and 13), and (ii) decreasing volumes of brecciated Types 1 and 2 block from the roof of the shear zone toward the footwall (Locatelli et al., 2018). The systematic presence of metasomatic ultramafic rinds surrounding the dismembered breccia blocks (i.e., metasomatic fluids; Step E; Figures 12e and 13) indicates that the LSZ concentrated large-scale circulation of ultramafic fluids along the plate interface during the first stages of exhumation of the Monviso slice, as proposed by Angiboust et al. (2014). Similar shear zones collecting slab-derived fluids have been reported in Syros melange (Breeding et al., 2004), Sesia zone (Konrad-Schmolke et al., 2011), Mont Emilius Arbolla shear zone (Angiboust et al., 2017), and Cima di Gagnone (e.g., Scambelluri et al., 2014).

9.3. Assessing the Role of Fluids in Transient Brittle Deformation

Geochemical results indicate that stepwise brecciation happened in the presence of a fluid, either locally derived (from surrounding metagabbros: Veins V0 and V1 and matrix M1) or mostly externally derived (from serpentinites: e.g., Vein V2 and M2 and M3 matrices), but the question remains: Did this fluid trigger brecciation or was it added as a result of permeability increase? While the mylonitic foliation of eclogite clasts suggests the prevalence of ductile deformation, during the prograde path Monviso metagabbros recorded several discrete events of brittle deformation (in both the LSZ and ISZ) along the prograde and retrograde paths. These are witnessed at various scales by fractured and sealed garnets, veins, and breccias crosscutting the mylonitic foliation (Angiboust, Langdon, et al., 2012; Broadwell et al., 2019; Locatelli et al., 2018) and could be attributed to changes in strain rate and/or fluid pressure (Angiboust, Langdon, et al., 2012).

Geochemical fingerprinting suggests that the formation of the M1 matrix (Figures 5, 7a, 7b, and 7d; see section 9.1.2) coincided with the garnet-in and lawsonite/glaucophane-out dehydration reactions (Figures 10b and 10c) in the thin intermediate metagabbro layers surrounding the Fe-Ti breccia planes. Since the latter reaction is predicted to occur across a very restricted P–T range (Figure 10c), it is likely to have produced a fluid pulse and may conceivably have induced brecciation by dehydration embrittlement. This would be consistent with the record of acoustic emissions spatially correlated to crack formation during the crossing of the glaucophane-out reaction in experiments studying the eclogitization of lawsonite-blueschists (at confining pressure of 2.5 GPa; Incel et al., 2017). But the authors, based on the presence of nanometric, newly formed omphacite grains on fracture and shear band walls, argued for a process of transformational faulting rather than dehydration embrittlement. They also did not record acoustic emissions spatially linked to fracture development during the lawsonite-out reaction, contrary to Okazaki and Hirth (2016) who had argued for dehydration embrittlement. In the absence of preserved microtextures (such as fine-grained reaction products, likely annihilated with time), it remains somehow difficult to conclude on dehydration embrittlement or transformational faulting for LSZ brecciation.

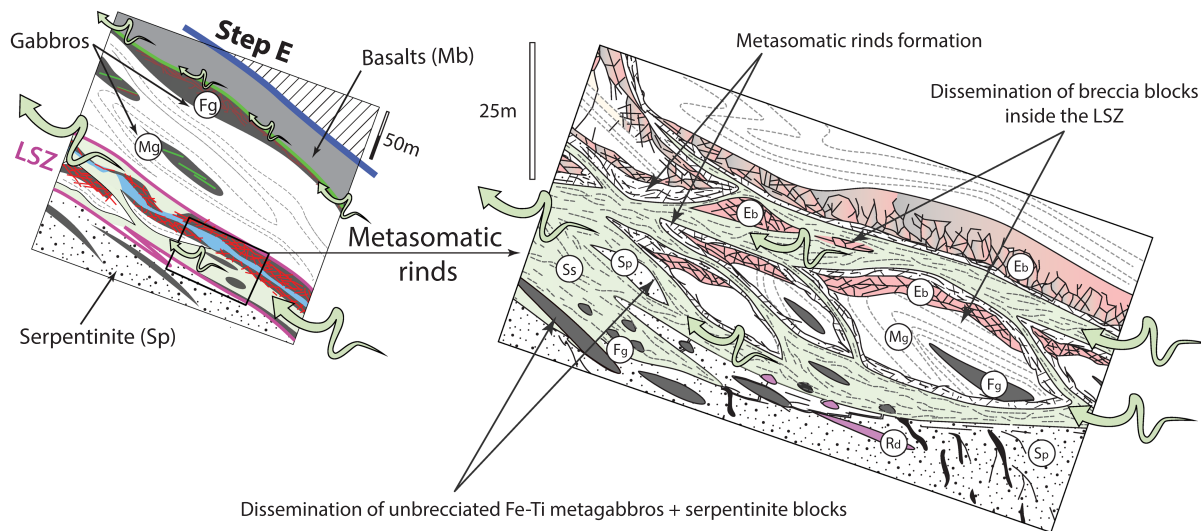


Figure 13. Scheme of fluid migration pathways in the LSZ at the onset of metasomatism, once breccia blocks were dismembered and embedded in the serpentinite-rich matrix of the LSZ (step E, coinciding with the exhumation of the LSU). The protracted fluid circulation throughout the LSZ led to (i) formation of new HP “late-stage veins” and (ii) extensive ultramafic metasomatism that affected brecciated blocks with prominent rind formation. The interplay between ongoing deformation and fluid-assisted metasomatism likely decreased the strength of the rock, promoting the widening of the shear zone and the incorporation of breccia blocks and metagabbros slivers into the serpentinitized LSZ. Base figure modified after Konrad-Schmolke et al. (2011). Mb = metabasites; Eb = eclogitic breccia; Ss = antigorite-rich schists of LSZ; Fg = Fe-Ti metagabbros; mg = mg-Al metagabbros; Mp = serpentinitized metaperidotites; Rd = rodingitic dykes; Bs = basal serpentinites.

Worthy of note, the same glaucophane-out reaction in the Fe-Ti metagabbros (which happened at somewhat lower P-T conditions on the prograde path; Locatelli et al., 2018) did not trigger brecciation but only intense garnet fracturing (Broadwell et al., 2019) and the formation of numerous omphacite veins V0 (predating brecciation and with Omp1b composition suggesting local equilibrium: Step A; Figure 11a; Philippot and Selverstone, 1991; Spandler et al., 2011). These veins crosscut the mylonitic foliation and even entire Fe-Ti boudins in places but remain as discrete, localized, and unconnected brittle structures compared to the M1 breccia planes. This raises the question of which parameters control the development of brecciation versus veining “only” for very similar fluid-releasing (negative ΔV) prograde reactions. Competing rates of reaction (and associated fluid release) versus strain may be a critical parameter (e.g., as suggested by acoustic emissions depending on the imposed P-T path; Incel et al., 2019) and slight variations in P-T paths and/or bulk rock composition (e.g., lawsonite-out reaction in blueschist; Incel et al., 2017; pure lawsonite composition; Okazaki & Hirth, 2016) may thus partly control the onset of brittle behaviour in otherwise ductile conditions. Strong rheological contrasts also partly controlled brecciation in the LSZ, as suggested by localization of breccia planes exclusively at the contact between ductilely deforming, still hydrated, garnet-poor intermediate metagabbro (Figures 2b and 2c) and already dry and stronger Fe-Ti metagabbro boudins (i.e., composed of garnet + omphacite; Locatelli et al., 2018). Lower rheological contrasts along the prograde path (e.g., lower garnet content in Fe-Ti metagabbros) possibly impeded brecciation before peak conditions.

To summarize our preferred interpretation, (i) M1 brecciation results from an internally controlled process and could therefore be attributed to either dehydration embrittlement or transformational faulting (i.e. fluids acting as a driver) and (ii) M3 brecciation, in contrast, marks fluid ingress during the widening of the LSZ (which was previously weakened by M1 and M2): at that stage kilometer-scale connectivity is fully effective, which for example suggests that fluids permeate into existing fracture networks ingress (i.e. fluids are a consequence) rather than drive local dehydration embrittlement.

Formation of M2 is more uncertain: It could be viewed as either locally controlled (i.e., meter to decameter-scale assuming that equilibrium fluids derive from the dehydration of some combination of Intermediate metagabbros and adjacent serpentinites via the brucite-out reaction; e.g., Gilio, 2017) or reflecting ingress of deeper, ultramafic fluids as a prelude to M3.

10. Conclusions

We herein show how the Monviso LSZ brecciated blocks record the stepwise development of a major subduction shear zone, from incipient brecciation to a ≥ 100 -m wide shear zone interconnected over >10 km, via progressive strain localization and increase in permeability and in the scale of fluid circulation. Geochemical data on the successive vein and matrix generations reveal a progressive opening of the system, from centimeter-scale interactions with a locally released fluid, to increasing amounts of external fluids and finally into km-scale infiltration (of serpentinite-derived fluids).

Development of the shear zone reveals a complex interplay of fluid release (through dehydration reactions) at rheological contrasts, brittle deformation events, and external fluid influx. In this framework, the successive fluid pulses recognized here reflect quite different processes: (i) M1 brecciation is likely associated with the onset, within the rock, of the garnet-in and glaucophane-out dehydration reactions and hint toward either dehydration embrittlement or transformational faulting; (ii) M3 brecciation, in contrast, marks fluid ingress during the widening of the LSZ, once a kilometer-scale connectivity is established; and (iii) the significance of M2 is more uncertain and could reflect a transitional stage between them, at the meter to decameter scale.

Eclogite-facies brecciation appears to have controlled the initial stages of strain localization within the LSZ and the ISZ (M1 and M2 events) and the further weakening and achievement of kilometer-scale connectivity in the LSZ (M3 event). This confirms the importance, in ductility deforming eclogite-facies rocks, of brittle deformation events for both strain localization processes and large-scale fluid circulation. If our interpretation is correct, the eclogite-facies breccias from Monviso may represent, together with healed eclogitic fractures in mylonitic garnets, the rock record of intermediate-depth tremors, as suggested by acoustic emissions observed in experiments during the glaucophane-out reaction.

Appendix A: Rationale of Field and Analytical Methods

The complete data set with geochemical data supporting this work (SM5) is available on figshare (10.6084/m9.figshare.9971813).

The geological mapping of the Monviso metaophiolite (Figures 1b–1d) results from original fieldwork at 1:10,000 scale using the topographic base of the Carta Tecnica Regionale (CTR maps) of the Regione Piemonte, Italy. The geological cross sections (showing the internal geometries of the metaophiolite and the shear zones; Figures 1e, 1f, and 13b) are drawn on topographic profiles from the DTM provided by the Regione Piemonte. The new lithological, structural, and geomorphological data were compared and locally integrated with those from Balestro et al. (2013) and Lombardo (1978).

The precise location of metagabbro blocks was obtained by GPS positioning (latitude, longitude, and altitude); the petrographic, structural, and geochemical analyses were performed on those with preserved chronological relationships between veins and matrices. Major focus was given to the blocks with preserved contacts with the shear zone matrix foliation.

To achieve high sampling precision and minimize the outcrop destruction, 55 samples of brecciated blocks were drilled inside eclogite-facies blocks for subsequent petrographic and geochemical analysis. Of those, 27 samples of clasts, veins, and matrices of eclogite-facies breccias from both the LSZ and ISZ were selected for bulk-rock major and trace element analysis, as well as in situ major and trace element analyses on minerals, coupled to macrostructural and microstructural study of eclogitic breccias. In addition to the metagabbros (both Mg-Al and Fe-Ti, intact and brecciated), metasomatic rinds postdating brecciation, antigorite schists forming the matrix of the shear zones and blocks of serpentinitized peridotite were analyzed. The microstructural study at the thin section scale was performed using both optical microscope and SEM (Zeiss Supra 55VP associated to SSD detector PTG Sahara for EDS analysis; ISTE_P, UPMC). Mineral chemical compositions (major element) were then analyzed by EPMA (CAMECA FIVE and SX100) at CAMPARIS (UPMC, Paris). The detailed workflow followed for the geochemical analysis (from sample preparation to data processing) is exhaustively described on paragraph 4. For more details on field mapping and structural analysis refer to Locatelli et al. (2018, 2019).

Acknowledgments

This study was funded by the project “Zooming in Between Plates” (Marie Curie International Training Network of the European Union’s Seventh Framework Program FP7/2007-2013/ under REA grant agreement no. 604713). We thank M. Fialin, N. Rividi (CAMPARIS) and O. Boudouma (ISTeP) for their analytical support and E. Delairis (ISTeP) for the preparation of thin sections. Technicians of SARM-CRPG (Nancy, France) and Hubert Whitechurch (University of Strasbourg) are thanked for the help given in bulk-rock chemical analyses. A special mention is for the friends of Rifugio Alpetto, which provided an invaluable support during fieldwork. Stephane Guillot and Gianluca Vignaroli are warmly thanked for their constructive reviews and suggestions and Claudio Faccenna for his editorial handling leading to a significant improvement of the manuscript.

References

- Abers, G. A., Nakajima, J., van Keken, P. E., Kita, S., & Hacker, B. R. (2013). Thermal-petrological controls on the location of earthquakes within subducting plates. *Earth and Planetary Science Letters*, 369–370, 178–187. <https://doi.org/10.1016/j.epsl.2013.03.022>
- Agard, P., Monié, P., Jolivet, L., & Goffé, B. (2002). Exhumation of the Schistes Lustrés complex: In situ laser probe ⁴⁰Ar/³⁹Ar constraints and implications for the Western Alps. *Journal of Metamorphic Geology*, 20(6), 599–618. <https://doi.org/10.1046/j.1525-1314.2002.00391.x>
- Agard, P., Plunder, A., Angiboust, S., Bonnet, G., & Ruh, J. (2018). The subduction plate interface: Rock record and mechanical coupling (from long to short timescales). *Lithos*, 320–321, 537–566. <https://doi.org/10.1016/j.lithos.2018.09.029>
- Agard, P., Yamato, P., Jolivet, L., & Burov, E. (2009). Exhumation of oceanic blueschists and eclogites in subduction zones: Timing and mechanisms. *Earth Science Reviews*, 92(1–2), 53–79. <https://doi.org/10.1016/j.earscirev.2008.11.002>
- Angiboust, S., Agard, P., Raimbourg, H., Yamato, P., & Huet, B. (2011). Subduction interface processes recorded by eclogite-facies shear zones (Monviso, W. Alps). *Lithos*, 127(1–2), 222–238. <https://doi.org/10.1016/j.lithos.2011.09.004>
- Angiboust, S., Agard, P., Yamato, P., & Raimbourg, H. (2012). Eclogite breccias in a subducted ophiolite: A record of intermediate-depth earthquakes? *Geology*, 40(8), 707–710. <https://doi.org/10.1130/G32925.1>
- Angiboust, S., Langdon, R., Agard, P., Waters, D., & Chopin, C. (2012). Eclogitization of the Monviso ophiolite (W. Alps) and implications on subduction dynamics: Monviso eclogites and subduction dynamics. *Journal of Metamorphic Geology*, 30(1), 37–61. <https://doi.org/10.1111/j.1525-1314.2011.00951.x>
- Angiboust, S., Pettke, T., Hoog, J. C. M. D., Caron, B., & Oncken, O. (2014). Channelized fluid flow and eclogite-facies metasomatism along the subduction shear zone. *Journal of Petrology*, 55(5), 883–916. <https://doi.org/10.1093/petrology/egu010>
- Angiboust, S., Yamato, P., Hertgen, S., Hyppolito, T., Bebout, G. E., & Morales, L. (2017). Fluid pathways and high-P metasomatism in a subducted continental slice (Mt. Emilius klippe, W. Alps). *Journal of Metamorphic Geology*, 35(5), 471–492. <https://doi.org/10.1111/jmg.12241>
- Audet, P., Bostock, M. G., Christensen, N. I., & Peacock, S. M. (2009). Seismic evidence for overpressured subducted oceanic crust and megathrust fault sealing. *Nature*, 457(7225), 76–78. <https://doi.org/10.1038/nature07650>
- Austrheim, H. (1987). Eclogitization of lower crustal granulites by fluid migration through shear zones. *Earth and Planetary Science Letters*, 81(2–3), 221–232. [https://doi.org/10.1016/0012-821X\(87\)90158-0](https://doi.org/10.1016/0012-821X(87)90158-0)
- Auzanneau, E., Schmidt, M. W., Vielzeuf, D., & Connolly, J. A. D. (2009). Titanium in phengite: A geobarometer for high temperature eclogites. *Contributions to Mineralogy and Petrology*, 159(1), 1–24. <https://doi.org/10.1007/s00410-009-0412-7>
- Bach, W., Alt, J. C., Niu, Y., Humphris, S. E., Erzinger, J., & Dick, H. J. B. (2001). The geochemical consequences of late-stage low-grade alteration of lower ocean crust at the SW Indian ridge: Results from ODP hole 735B (leg 176). *Geochimica et Cosmochimica Acta*, 65(19), 3267–3287. [https://doi.org/10.1016/S0016-7037\(01\)00677-9](https://doi.org/10.1016/S0016-7037(01)00677-9)
- Balestro, G., Fioraso, G., & Lombardo, B. (2013). Geological map of the Monviso massif (Western Alps). *Journal of Maps*, 9(4), 623–634. <https://doi.org/10.1080/17445647.2013.842507>
- Balestro, G., Lombardo, B., Vaggelli, G., Borghi, A., Festa, A., & Gattiglio, M. (2014). Tectonostratigraphy of the northern Monviso meta-ophiolite complex (Western Alps). *Italian Journal of Geosciences*, 133(3), 409–426. <https://doi.org/10.3301/IJG.2014.13>
- Bebout, G. E., & Barton, M. D. (1993). Metasomatism during subduction: Products and possible paths in the Catalina schist, California. *Chem. Geol., Fluid-rock Interaction in the Deeper Continental Lithosphere*, 108(1–4), 61–92. [https://doi.org/10.1016/0009-2541\(93\)90318-D](https://doi.org/10.1016/0009-2541(93)90318-D)
- Blake, M. C. Jr., Moore, D. E., & Jayko, A. S. (1995). The role of serpentinite melanges in the unroofing of UHPM rocks: An example from the Western Alps of Italy. *Ultrahigh Pressure Metamorphism*, 182–205. <https://doi.org/10.1017/CBO9780511573088.007>
- Bodinier, J. L., & Godard, M. (2003). Orogenic, ophiolitic, and abyssal peridotites. *Treatise on geochemistry*, 2, 568.
- Brace, W. F. (1984). Permeability of crystalline rocks: New in situ measurements. *Journal of Geophysical Research - Solid Earth*, 89(B6), 4327–4330. <https://doi.org/10.1029/JB089iB06p04327>
- Breeding, C. M., Ague, J. J., & Bröcker, M. (2004). Fluid-metasedimentary rock interactions in subduction-zone mélange: Implications for the chemical composition of arc magmas. *Geology*, 32(12), 1041–1044. <https://doi.org/10.1130/G20877.1>
- Broadwell, K. S., Locatelli, M., Verlaquet, A., Agard, P., & Caddick, M. J. (2019). Transient and periodic brittle deformation of eclogites during intermediate-depth subduction. *Earth and Planetary Science Letters*, 521, 91–102. <https://doi.org/10.1016/j.epsl.2019.06.008>
- Bromiley, G. D., & Pawley, A. R. (2003). The stability of antigorite in the systems MgO-SiO₂-H₂O (MSH) and MgO-Al₂O₃-SiO₂-H₂O (MASH): The effects of Al₃₊ substitution on high-pressure stability. *American Mineralogist*, 88(1), 99–108. <https://doi.org/10.2138/am-2003-0113>
- Brudzinski, M. R., Thurber, C. H., Hacker, B. R., & Engdahl, E. R. (2007). Global prevalence of double benioff zones. *Science*, 316(5830), 1472–1474. <https://doi.org/10.1126/science.1139204>
- Bucholz, C. E., & Ague, J. J. (2010). Fluid flow and Al transport during quartz-kyanite vein formation, Unst, Shetland Islands, Scotland. *Journal of Metamorphic Geology*, 28(1), 19–39. <https://doi.org/10.1111/j.1525-1314.2009.00851.x>
- Carignan, J., Hild, P., Mevelle, G., Morel, J., & Yeghicheyan, D. (2001). Routine analyses of trace elements in geological samples using flow injection and low pressure on-line liquid chromatography coupled to ICP-MS: A study of geochemical reference materials BR, DR-N, UB-N, AN-G and GH. *Geostandards Newsletter*, 25(2–3), 187–198. <https://doi.org/10.1111/j.1751-908X.2001.tb00595.x>
- Carmichael, I. S. E. (1964). The petrology of Thingmuli, a tertiary volcano in eastern Iceland. *Journal of Petrology*, 5(3), 435–460. <https://doi.org/10.1093/petrology/5.3.435>
- Castelli, D., Rostagno, C., & Lombardo, B. (2002). JD-QTZ-bearing metaplagiogranite from the Monviso meta-ophiolite (western Alps). *Ophioliti*, 27, 81–90. <https://doi.org/10.4454/ofioliti.v27i2.178>
- Codillo, E. A., Le Roux, V., & Marschall, H. R. (2018). Arc-like magmas generated by mélange-peridotite interaction in the mantle wedge. *Nature Communications*, 9(1), 1–11. <https://doi.org/10.1038/s41467-018-05313-2>
- Coggon, R., & Holland, T. J. B. (2002). Mixing properties of phengitic micas and revised garnet-phengite thermobarometers. *Journal of Metamorphic Geology*, 20(7), 683–696. <https://doi.org/10.1046/j.1525-1314.2002.00395.x>
- Connolly, J. A. D. (1990). Multivariable phase diagrams; an algorithm based on generalized thermodynamics. *American Journal of Science*, 290(6), 666–718. <https://doi.org/10.2475/ajs.290.6.666>
- Connolly, J. A. D. (2005). Computation of phase equilibria by linear programming: A tool for geodynamic modeling and its application to subduction zone decarbonation. *Earth and Planetary Science Letters*, 236(1–2), 524–541. <https://doi.org/10.1016/j.epsl.2005.04.033>
- Connolly, J. A. D. (2010). The mechanics of metamorphic fluid expulsion. *Elements*, 6(3), 165–172. <https://doi.org/10.2113/gselements.6.3.165>

- Davies, J. H. (1999). The role of hydraulic fractures and intermediate-depth earthquakes in generating subduction-zone magmatism. *Nature*, *398*(6723), 142–145. <https://doi.org/10.1038/18202>
- Defant, M. J., & Drummond, M. S. (1990). Derivation of some modern arc magmas by melting of young subducted lithosphere. *Nature*, *347*(6294), 662–665. <https://doi.org/10.1038/347662a0>
- Deschamps, F., Godard, M., Guillot, S., & Hattori, K. (2013). Geochemistry of subduction zone serpentinites: A review. *Lithos*, *Serpentinites from mid-oceanic ridges to subduction*, *178*, 96–127. <https://doi.org/10.1016/j.lithos.2013.05.019>
- Diener, J. F. A., Powell, R., White, R. W., & Holland, T. J. B. (2007). A new thermodynamic model for clino- and orthoamphiboles in the system $\text{Na}_2\text{O}?\text{CaO}?\text{FeO}?\text{MgO}?\text{Al}_2\text{O}_3?\text{SiO}_2?\text{H}_2\text{O}?\text{O}$. *Journal of Metamorphic Geology*, *25*(6), 631–656. <https://doi.org/10.1111/j.1525-1314.2007.00720.x>
- Festa, A., Balestro, G., Dilek, Y., & Tartarotti, P. (2015). A Jurassic oceanic core complex in the high-pressure Monviso ophiolite (Western Alps, NW Italy). *Lithosphere*, *7*, 646–652. <https://doi.org/10.1130/L458.1>
- Festa, A., Pini, G. A., Ogata, K., & Dilek, Y. (2019). Diagnostic features and field-criteria in recognition of tectonic, sedimentary and diapiric mélanges in orogenic belts and exhumed subduction-accretion complexes. *Gondwana Research*, *74*, 7–30. <https://doi.org/10.1016/j.gr.2019.01.003>
- Fuhrman, M. L., & Linsley, D. H. (1988). Ternary-feldspar modeling and thermometry. *American Mineralogist*, *73*, 201–215.
- Fumagalli, P., & Poli, S. (2004). Experimentally determined phase relations in hydrous peridotites to 6.5 GPa and their consequences on the dynamics of subduction zones. *Journal of Petrology*, *46*(3), 555–578.
- Gao, J., John, T., Klemd, R., & Xiong, X. (2007). Mobilization of Ti-Nb-Ta during subduction: Evidence from rutile-bearing dehydration segregations and veins hosted in eclogite, Tianshan, NW China. *Geochimica et Cosmochimica Acta*, *71*(20), 4974–4996. <https://doi.org/10.1016/j.gca.2007.07.027>
- Gilio, M. (2017). Alpine serpentinite: A key to unravel subduction accretion at the plate interface. *Plinius*, *43*, 57–65. <https://doi.org/10.19276/plinius.2017.01007>
- Glodny, J., Austrheim, H., Molina, J. F., Rusin, A. I., & Seward, D. (2003). Rb/Sr record of fluid-rock interaction in eclogites: The Marun-Keu complex, polar Urals, Russia. *Geochimica et Cosmochimica Acta*, *67*(22), 4353–4371. [https://doi.org/10.1016/S0016-7037\(03\)00370-3](https://doi.org/10.1016/S0016-7037(03)00370-3)
- Green, E., Holland, T., & Powell, R. (2007). An order-disorder model for omphacitic pyroxenes in the system jadeite-diopside-hedenbergite-acmite, with applications to eclogitic rocks. *American Mineralogist*, *92*, 1181–1189. <https://doi.org/10.2138/am.2007.2401>
- Groppo, C., & Castelli, D. (2010). Prograde P-T evolution of a Lawsonite Eclogite from the Monviso meta-ophiolite (Western Alps): Dehydration and redox reactions during subduction of oceanic feti-oxide gabbro. *Journal of Petrology*, *51*(12), 2489–2514. <https://doi.org/10.1093/ptrology/egq065>
- Groppo, C., & Compagnoni, R. (2007). Metamorphic veins from the serpentinites of the Piemonte zone, western Alps, Italy: A review. *Periodico di Mineralogia*, *76*, 127–153.
- Guillong, M., Meier, D. L., Allan, M. M., Heinrich, C. A., & Yardley, B. W. (2008). Appendix A6: SILLS: A MATLAB-based program for the reduction of laser ablation ICP-MS data of homogeneous materials and inclusions. *Mineralogical Association of Canada Short Course*, *40*, 328–333.
- Guillot, S., Schwartz, S., Hattori, K. H., Auzende, A. L., & Lardeaux, J. M. (2004). The Monviso ophiolitic massif (Western Alps), a section through a serpentinite subduction channel. *Journal of the Virtual Explorer* Electronic Ed, *16*. <https://doi.org/10.3809/jvirtex.2004.00099>
- Hacker, B. R. (2008). H_2O subduction beyond arcs. *Geochemistry, Geophysics, Geosystems*, *9*, Q03001. <https://doi.org/10.1029/2007GC001707>
- Hacker, B. R., Abers, G. A., & Peacock, S. M. (2003). Subduction factory 1. Theoretical mineralogy, densities, seismic wave speeds, and H_2O contents: Subduction zone mineralogy and physical properties. *Journal of Geophysical Research - Solid Earth*, *108*. <https://doi.org/10.1029/2001JB001127>
- Hacker, B. R., Peacock, S. M., Abers, G. A., & Holloway, S. D. (2003). Subduction factory 2. Are intermediate-depth earthquakes in subducting slabs linked to metamorphic dehydration reactions? *Journal of Geophysical Research - Solid Earth*, *108*, 2030. <https://doi.org/10.1029/2001JB001129>
- Halama, R., Konrad-Schmolke, M., Sudo, M., Marschall, H. R., & Wiedenbeck, M. (2014). Effects of fluid-rock interaction on $^{40}\text{Ar}/^{39}\text{Ar}$ geochronology in high-pressure rocks (Sesia-Lanzo zone, Western Alps). *Geochimica et Cosmochimica Acta*, *126*, 475–494. <https://doi.org/10.1016/j.gca.2013.10.023>
- Hattori, K. H., & Guillot, S. (2007). Geochemical character of serpentinites associated with high- to ultrahigh-pressure metamorphic rocks in the Alps, Cuba, and the Himalayas: Recycling of elements in subduction zones. *Geochemistry, Geophysics, Geosystems*, *8*, Q09010. <https://doi.org/10.1029/2007GC001594>
- Hermann, J., Spandler, C., Hack, A., & Korsakov, A. (2006). Aqueous fluids and hydrous melts in high-pressure and ultra-high pressure rocks: Implications for element transfer in subduction zones. *Lithos*, *92*(3–4), 399–417. <https://doi.org/10.1016/j.lithos.2006.03.055>
- Hergarten, S., Yamato, P., Morales, L. F. G., & Angiboust, S. (2017). Evidence for brittle deformation events at eclogite-facies P-T conditions (example of the Mt. Emilius klippe, Western Alps). *Tectonophysics*, *706*–*707*, 1–13. <https://doi.org/10.1016/j.tecto.2017.03.028>
- Holland, T., & Powell, R. (1991). A compensated-Redlich-Kwong (CORK) equation for volumes and fugacities of CO_2 and H_2O in the range 1 bar to 50 kbar and 100–1600 °C. *Contributions to Mineralogy and Petrology*, *109*(2), 265–273. <https://doi.org/10.1007/BF00306484>
- Holland, T., & Powell, R. (2003). Activity?Composition relations for phases in petrological calculations: An asymmetric multicomponent formulation. *Contributions to Mineralogy and Petrology*, *145*(4), 492–501. <https://doi.org/10.1007/s00410-003-0464-z>
- Holland, T. J. B., & Powell, R. (1998). An internally consistent thermodynamic data set for phases of petrological interest. *Journal of Metamorphic Geology*, *16*, 309–343.
- Incel, S., Hilalret, N., Labrousse, L., John, T., Deldicque, D., Ferrand, T., et al. (2017). Laboratory earthquakes triggered during eclogitization of lawsonite-bearing blueschist. *Earth and Planetary Science Letters*, *459*, 320–331. <https://doi.org/10.1016/j.epsl.2016.11.047>
- Incel, S., Labrousse, L., Hilalret, N., John, T., Gasc, J., Shi, F., et al. (2019). Reaction-induced embrittlement of the lower continental crust. *Geology*, *47*(3), 235–238. <https://doi.org/10.1130/G45527.1>
- John, T., Gussone, N., Podladchikov, Y. Y., Bebout, G. E., Dohmen, R., Halama, R., et al. (2012). Volcanic arcs fed by rapid pulsed fluid flow through subducting slabs. *Nature Geoscience*, *5*(7), 489–492. <https://doi.org/10.1038/ngeo1482>
- John, T., & Schenk, V. (2006). Interrelations between intermediate-depth earthquakes and fluid flow within subducting oceanic plates: Constraints from eclogite facies pseudotachylytes. *Geology*, *34*(7), 557–560. <https://doi.org/10.1130/G22411.1>
- Kodolányi, J., Pettke, T., Spandler, C., Kamber, B. S., & Gmélning, K. (2012). Geochemistry of ocean floor and fore-arc serpentinites: Constraints on the ultramafic input to subduction zones. *Journal of Petrology*, *53*(2), 235–270. <https://doi.org/10.1093/ptrology/egr058>

- Konrad-Schmolke, M., Zack, T., O'Brien, P. J., & Barth, M. (2011). Fluid migration above a subducted slab—Thermodynamic and trace element modelling of fluid-rock interaction in partially overprinted eclogite-facies rocks (Sesia Zone, Western Alps). *Earth and Planetary Science Letters*, 311(3-4), 287–298. <https://doi.org/10.1016/j.epsl.2011.09.025>
- Kostenko, O., Jamtveit, B., Austrheim, H., Pollok, K., & Putnis, C. (2002). The mechanism of fluid infiltration in peridotites at Almklovdalen, western Norway. *Geofluids*, 2(3), 203–215. <https://doi.org/10.1046/j.1468-8123.2002.00038.x>
- Lardeaux, J. M., Nisio, P., & Boudeulle, M. (1987). Deformational and metamorphic history at the Lago Superiore area of the Monviso ophiolitic complex (Italian Western Alps): A record of subduction–collision cycle. *Ophioliti*, 12, 479–502.
- Lifshin, E., & Gauvin, R. (2001). Minimizing errors in electron microprobe analysis. *Microscopy and Microanalysis. Microscopy and Microanalysis*, 7, 168–177. <https://doi.org/10.1007/S100050010084>
- Locatelli, M., Federico, L., Agard, P., & Verlaguet, A. (2019). Geology of the southern Monviso metaophiolite complex (W-Alps, Italy). *Journal of Maps*, 15(2), 283–297. <https://doi.org/10.1080/17445647.2019.1592030>
- Locatelli, M., Verlaguet, A., Agard, P., Federico, L., & Angiboust, S. (2018). Intermediate-depth brecciation along the subduction plate interface (Monviso eclogite, W. Alps). *Lithos*, 320–321, 378–402. <https://doi.org/10.1016/j.lithos.2018.09.028>
- Lombardo, B. (1978). Osservazioni preliminari sulle ofioliti metamorfiche del Monviso (Alpi Occidentali). *Rendiconti Della Soc. Ital. Mineral. E Petrol.*, 34, 235–305.
- Lund, M. G., & Austrheim, H. (2003). High-pressure metamorphism and deep-crustal seismicity: Evidence from contemporaneous formation of pseudotachylytes and eclogite facies coronas. *Tectonophysics*, 372(1-2), 59–83. [https://doi.org/10.1016/S0040-1951\(03\)00232-4](https://doi.org/10.1016/S0040-1951(03)00232-4)
- Mancktelow, N. S., & Pennacchioni, G. (2005). The control of precursor brittle fracture and fluid-rock interaction on the development of single and paired ductile shear zones. *Journal of Structural Geology*, 27(4), 645–661. <https://doi.org/10.1016/j.jsg.2004.12.001>
- Marschall, H. R., & Schumacher, J. C. (2012). Arc magmas sourced from mélange diapirs in subduction zones. *Nature Geoscience*, 5(12), 862–867. <https://doi.org/10.1038/ngeo1634>
- Marthaler, M., & Stampfli, G. M. (1989). Les Schistes lustrés à ophiolites de la nappe du Tsaté: Un ancien prisme d'accrétion issu de la marge active apulienne? *Schweiz. Mineral. Petrogr. Mitteilungen*, 69, 211–216.
- Martin, L. A. J., Hermann, J., Gauthiez-Putallaz, L., Whitney, D. L., Vitale Brovarone, A., Fornash, K. F., & Evans, N. J. (2014). Lawsonite geochemistry and stability—implication for trace element and water cycles in subduction zones. *Journal of Metamorphic Geology*, 32(5), 455–478.
- Manzotti, P., Ballèvre, M., & Dal Piaz, G. V. (2017). Continental gabbros in the Dent Blanche Tectonic System (Western Alps): from the pre-Alpine crustal structure of the Adriatic palaeo-margin to the geometry of an alleged subduction interface. *Journal of the Geological Society*, 174(3), 541–556.
- McDonough, W., Albarede, F., Staudigel, H., & White, B. (1996). Geoscientists unite to develop earth reference model. *EOS. Transactions of the American Geophysical Union*, 77(45), 443. <https://doi.org/10.1029/96EO00298>
- Messiga, Kienast, Rebay, Riccardi, & Tribuzio (1999). Cr-rich magnesiochloritoid eclogites from the Monviso ophiolites (Western Alps, Italy). *Journal of Metamorphic Geology*, 17(3), 287–299. <https://doi.org/10.1046/j.1525-1314.1999.00198.x>
- Mibe, K., Yoshino, T., Ono, S., Yasuda, A., & Fujii, T. (2003). Connectivity of aqueous fluid in eclogite and its implications for fluid migration in the Earth's interior. *Journal of Geophysical Research - Solid Earth*, 108(B6), 2295. <https://doi.org/10.1029/2002JB001960>
- Morrow, C. A., Shi, L. Q., & Byerlee, J. D. (1984). Permeability of fault gouge under confining pressure and shear stress. *Journal of Geophysical Research - Solid Earth*, 89(B5), 3193–3200. <https://doi.org/10.1029/JB089iB05p03193>
- Nadeau, S., Philippot, P., & Pineau, F. (1993). Fluid inclusion and mineral isotopic compositions (HCO) in eclogitic rocks as tracers of local fluid migration during high-pressure metamorphism. *Earth and Planetary Science Letters*, 114(4), 431–448. [https://doi.org/10.1016/0012-821X\(93\)90074-J](https://doi.org/10.1016/0012-821X(93)90074-J)
- Nakajima, J., Yoshida, K., & Hasegawa, A. (2013). An intraslab seismic sequence activated by the 2011 Tohoku-oki earthquake: Evidence for fluid-related embrittlement. *Journal of Geophysical Research: Solid Earth*, 118, 3492–3505. <https://doi.org/10.1002/jgrb.50246>
- Okazaki, K., & Hirth, G. (2016). Dehydration of lawsonite could directly trigger earthquakes in subducting oceanic crust. *Nature*, 530(7588), 81–84. <https://doi.org/10.1038/nature16501>
- Padrón-Navarta, J. A., Hermann, J., Garrido, C. J., Sánchez-Vizcaíno, V. L., & Gómez-Pugnaire, M. T. (2010). An experimental investigation of antigorite dehydration in natural silica-enriched serpentinite. *Contributions to Mineralogy and Petrology*, 159(1), 25.
- Pawley, A. R. (1994). The pressure and temperature stability limits of lawsonite: Implications for H₂O recycling in subduction zones. *Contributions to Mineralogy and Petrology*, 118(1), 99–108. <https://doi.org/10.1007/BF00310614>
- Peacock, S. M. (1993). Large-scale hydration of the lithosphere above subducting slabs. *Chemical Geology, Fluid-rock Interaction in the Deeper Continental Lithosphere*, 108(1-4), 49–59. [https://doi.org/10.1016/0009-2541\(93\)90317-C](https://doi.org/10.1016/0009-2541(93)90317-C)
- Pennacchioni, G., & Cesare, B. (1997). Ductile-brittle transition in pre-Alpine amphibolite facies mylonites during evolution from water-present to water-deficient conditions (Mont Mary nappe, Italian Western Alps). *Journal of Metamorphic Geology*, 15(6), 777–791. <https://doi.org/10.1111/j.1525-1314.1997.00055.x>
- Pennacchioni, G., & Mancktelow, N. S. (2007). Nucleation and initial growth of a shear zone network within compositionally and structurally heterogeneous granulites under amphibolite facies conditions. *Journal of Structural Geology*, 29(11), 1757–1780. <https://doi.org/10.1016/j.jsg.2007.06.002>
- Penniston-Dorland, S. C., Sorensen, S. S., Ash, R. D., & Khadke, S. V. (2010). Lithium isotopes as a tracer of fluids in a subduction zone mélange: Franciscan complex, CA. *Earth and Planetary Science Letters*, 292(1-2), 181–190. <https://doi.org/10.1016/j.epsl.2010.01.034>
- Peters, D., Bretscher, A., John, T., Scambelluri, M., & Pettke, T. (2017). Fluid-mobile elements in serpentinites: Constraints on serpentinisation environments and element cycling in subduction zones. *Chemical Geology*, 466, 654–666. <https://doi.org/10.1016/j.chemgeo.2017.07.017>
- Pettke, T., Oberli, F., Audétat, A., Guillong, M., Simon, A. C., Hanley, J. J., & Klemm, L. M. (2012). Recent developments in element concentration and isotope ratio analysis of individual fluid inclusions by laser ablation single and multiple collector ICP-MS. *Ore Geology Reviews*, 44, 10–38. <https://doi.org/10.1016/j.oregeorev.2011.11.001>
- Philippot, P. (1987). “Crack seal” vein geometry in eclogitic rocks. *Geodinamica Acta*, 1(3), 171–181. <https://doi.org/10.1080/09853111.1987.11105136>
- Philippot, P., & Kienast, J.-R. (1989a). Chemical-microstructural changes in eclogite-facies shear zones (Monviso, Western Alps, North Italy) as indicators of strain history and the mechanism of mass transfer. *Lithos*, 23(3), 179–200. [https://doi.org/10.1016/0024-4937\(89\)90004-2](https://doi.org/10.1016/0024-4937(89)90004-2)

- Philippot, P., & Kienast, J.-R. (1989b). Chemical-microstructural changes in eclogite-facies shear zones (Monviso, Western Alps, North Italy) as indicators of strain history and the mechanism and scale of mass transfer. *Lithos*, 23(3), 179–200. [https://doi.org/10.1016/0024-4937\(89\)90004-2](https://doi.org/10.1016/0024-4937(89)90004-2)
- Philippot, P., & Selverstone, J. (1991). Trace-element-rich brines in eclogitic veins: Implications for fluid composition and transport during subduction. *Contributions to Mineralogy and Petrology*, 106(4), 417–430. <https://doi.org/10.1007/BF00321985>
- Philippot, P., & van Roermund, H. L. M. (1992). Deformation processes in eclogitic rocks: Evidence for the rheological delamination of the oceanic crust in deeper levels of subduction zones. *Journal of Structural Geology*, Mechanical Instabilities in Rocks and Tectonics, 14(8–9), 1059–1077. [https://doi.org/10.1016/0191-8141\(92\)90036-V](https://doi.org/10.1016/0191-8141(92)90036-V)
- Plunder, A., Agard, P., Chopin, C., & Okay, A. I. (2013). Geodynamics of the Tavşanlı zone, western Turkey: Insights into subduction/obduction processes. *Tectonophysics*, 608, 884–903. <https://doi.org/10.1016/j.tecto.2013.07.028>
- Rubatto, D., & Hermann, J. (2003). Zircon formation during fluid circulation in eclogites (Monviso, Western Alps): Implications for Zr and Hf budget in subduction zones. *Geochimica et Cosmochimica Acta*, 67(12), 2173–2187. [https://doi.org/10.1016/S0016-7037\(02\)01321-2](https://doi.org/10.1016/S0016-7037(02)01321-2)
- Rupke, L. (2004). Serpentine and the subduction zone water cycle. *Earth and Planetary Science Letters*, 223(1–2), 17–34. <https://doi.org/10.1016/j.epsl.2004.04.018>
- Scambelluri, M., Fiebig, J., Malaspina, N., Müntener, O., & Pettko, T. (2004). Serpentinite subduction: Implications for fluid processes and trace-element recycling. *International Geology Review*, 46(7), 595–613. <https://doi.org/10.2747/0020-6814.46.7.595>
- Scambelluri, M., Pettko, T., Rampono, E., Godard, M., & Reusser, E. (2014). Petrology and trace element budgets of high-pressure peridotites indicate subduction dehydration of serpentinized mantle (Cima di Gagnone, Central Alps, Switzerland). *Journal of Petrology*, 55(3), 459–498. <https://doi.org/10.1093/petrology/egt068>
- Scambelluri, M., & Philippot, P. (2001). Deep fluids in subduction zones. *Lithos*, Fluid Inclusions: Phase Relationships - Methods - Applications. A Special Issue in honour of Jacques Touret, 55(1–4), 213–227. [https://doi.org/10.1016/S0024-4937\(00\)00046-3](https://doi.org/10.1016/S0024-4937(00)00046-3)
- Scambelluri, M., Strating, E. H. H., Piccardo, G. B., Vissers, R. L. M., & Rampono, E. (1991). Alpine olivine- and titanite clinohumite-bearing assemblages in the Erro-Tobbio peridotite (Voltri Massif, NW Italy). *Journal of Metamorphic Geology*, 9(1), 79–91. <https://doi.org/10.1111/j.1525-1314.1991.tb00505.x>
- Schmidt, M. W., & Poli, S. (1998). Experimentally based water budgets for dehydrating slabs and consequences for arc magma generation. *Earth and Planetary Science Letters*, 163(1–4), 361–379. [https://doi.org/10.1016/S0012-821X\(98\)00142-3](https://doi.org/10.1016/S0012-821X(98)00142-3)
- Schrank, C. E., Handy, M. R., & Füsseis, F. (2008). Multiscaling of shear zones and the evolution of the brittle-to-viscous transition in continental crust. *Journal of Geophysical Research - Solid Earth*, 113(B1), B01407. <https://doi.org/10.1029/2006JB004833>
- Schwartz, S., Lardeaux, J.-M., Guillot, S., & Tricart, P. (2000). Diversité du métamorphisme écolitique dans le massif ophiolitique du Monviso (Alpes occidentales, Italie). *Geodinamica Acta*, 13(2–3), 169–188. <https://doi.org/10.1080/09853111.2000.11105371>
- Shiina, T., Nakajima, J., & Matsuzawa, T. (2013). Seismic evidence for high pore pressures in the oceanic crust: Implications for fluid-related embrittlement. *Geophysical Research Letters*, 40, 2006–2010. <https://doi.org/10.1002/grl.50468>
- Sibson, R. H. (1977). Fault rocks and fault mechanisms. *Journal of the Geological Society*, 133(3), 191–213. <https://doi.org/10.1144/gsjgs.133.3.0191>
- Spandler, C., & Hermann, J. (2006). High-pressure veins in eclogite from New Caledonia and their significance for fluid migration in subduction zones. *Lithos*, 89(1–2), 135–153. <https://doi.org/10.1016/j.lithos.2005.12.003>
- Spandler, C., Hermann, J., Arculus, R., & Mavrogenes, J. (2003). Redistribution of trace elements during prograde metamorphism from lawsonite blueschist to eclogite facies; implications for deep subduction-zone processes. *Contributions to Mineralogy and Petrology*, 146(2), 205–222. <https://doi.org/10.1007/s00410-003-0495-5>
- Spandler, C., Pettko, T., & Rubatto, D. (2011). Internal and external fluid sources for eclogite-facies veins in the monviso meta-ophiolite, Western Alps: Implications for fluid flow in subduction zones. *Journal of Petrology*, 52(6), 1207–1236. <https://doi.org/10.1093/petrology/egr025>
- Spinelli, G. A., & Wang, K. (2009). Links between fluid circulation, temperature, and metamorphism in subducting slabs. *Geophysical Research Letters*, 36, L13302. <https://doi.org/10.1029/2009GL038706>
- Stern, R. J. (2002). Subduction zones. *Reviews of Geophysics*, 40(4), 1012. <https://doi.org/10.1029/2001RG000108>
- Sun, S.-s., & McDonough, W. F. (1989). Chemical and isotopic systematics of oceanic basalts: Implications for mantle composition and processes. *Geological Society of London, Special Publication*, 42(1), 313–345. <https://doi.org/10.1144/GSL.SP.1989.042.01.19>
- Ulmer, P., & Trommsdorff, V. (1995). Serpentine stability to mantle depths and subduction-related magmatism. *Science*, 268(5212), 858–861.
- Ulmer, P., & Trommsdorff, V. (1999). Phase relations of hydrous mantle subducting to 300 km. *Mantle Petrol. Field Obs. High Press. Exp. Tribute Francis RJoe Boyd*, 6, 259–281.
- van Keken, P. E., Hacker, B. R., Syracuse, E. M., & Abers, G. A. (2011). Subduction factory: 4. Depth-dependent flux of H₂O from subducting slabs worldwide. *Journal of Geophysical Research*, 116(B1). <https://doi.org/10.1029/2010JB007922>
- Watson, E. B., & Brenan, J. M. (1987). Fluids in the lithosphere, 1. Experimentally-determined wetting characteristics of CO₂-H₂O fluids and their implications for fluid transport, host-rock physical properties, and fluid inclusion formation. *Earth and Planetary Science Letters*, 85(4), 497–515.
- Wassmann, S., & Stöckhert, B. (2013). Low stress deformation of garnet by incongruent dissolution precipitation creep. *Journal of Structural Geology*, 46, 200–219. <https://doi.org/10.1016/j.jsg.2012.09.002>
- Widmer, T., & Thompson, A. B. (2001). Local origin of high pressure vein material in eclogite facies rocks of the Zermatt-Saas Zone, Switzerland. *American Journal of Science*, 301(7), 627–656. <https://doi.org/10.2475/ajs.301.7.627>
- Wong, T.-F., Ko, S.-C., & Olgaard, D. L. (1997). Generation and maintenance of pore pressure excess in a dehydrating system 2. Theoretical analysis. *Journal of Geophysical Research - Solid Earth*, 102(B1), 841–852. <https://doi.org/10.1029/96JB02484>
- Wood, D. A. (1979). A variably veined suboceanic upper mantle—Genetic significance for mid-ocean ridge basalts from geochemical evidence. *Geology*, 7(10), 499–503. [https://doi.org/10.1130/0091-7613\(1979\)7<499:AVVSUM>2.0.CO;2](https://doi.org/10.1130/0091-7613(1979)7<499:AVVSUM>2.0.CO;2)
- Yamasaki, T., & Seno, T. (2003). Double seismic zone and dehydration embrittlement of the subducting slab. *Journal of Geophysical Research - Solid Earth*, 108(B4), 2212. <https://doi.org/10.1029/2002JB001918>
- Zack, T., & John, T. (2007). An evaluation of reactive fluid flow and trace element mobility in subducting slabs. *Chemical Geology*, 239(3–4), 199–216. <https://doi.org/10.1016/j.chemgeo.2006.10.020>